Geomorphology 458 (2024) 109207

Contents lists available at ScienceDirect

Geomorphology

journal homepage: www.journals.elsevier.com/geomorphology

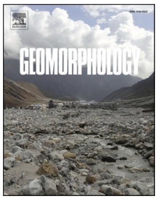

Subglacial bedform and moat initiation beneath Rutford Ice Stream, West Antarctica

Rebecca Schlegel [a,b,*], Alex M. Brisbourne [a], Andrew M. Smith [a], Adam D. Booth [c], Tavi Murray [b], Edward C. King [a], Roger A. Clark [c]

[a] *British Antarctic Survey, Natural Environment Research Council, Cambridge, UK*
[b] *Glaciology Group, Department of Geography, Swansea University, UK*
[c] *Institute of Applied Geoscience, School of Earth and Environment, University of Leeds, UK*

ARTICLE INFO

Keywords:
Elongated subglacial bedforms and moats
Bedform initiation and evolution
Modern Ice Stream
Rutford Ice Stream
West Antarctica
3D radar data
Acoustic impedance

ABSTRACT

The accuracy of sea-level rise predictions is highly dependent on reliably understanding the subglacial environment beneath ice streams. Bedforms result from the interaction between ice and its substrate, and therefore have the potential to shed light on poorly understood basal conditions influencing ice dynamics. However, theoretical models of bedform formation are often based on observations from deglaciated areas or from sparsely-sampled geophysical surveys over glaciated regions. Here, we use high-resolution three- and two-dimensional radar and seismic data to reveal details of the initiation and evolution of a subglacial bedform beneath Rutford Ice Stream, West Antarctica. Radar surveys at 20 m and 50 m line spacing allow detailed imaging of bed topography, including a moat up to 55 m deep, surrounding the upstream end of a 50-m high and >18-km long bedform. Many models rely on either a topographical or a locally resistant seed point to initiate bedform formation. The bedform described here is mostly composed of soft sediment (porosity >0.3) and lacks a boulder or outcrop, suggesting the bedform initiated without a topographic seed point. Sediment at the upstream end of bedforms appears stiffer over a distance of 2.3 km. We suggest sediment inhomogeneities in the initially flat bed cause the deposition of sediment, which, assuming resistant enough, acts as a seed point for bedform extension and moat erosion. The moat's geometry and its truncation of other bedforms suggest that it was eroded after the deposition of surrounding bedforms. These observations from a modern ice stream deliver information of subglacial processes involved in the initiation as well as *in situ* high-resolution topography and properties of bedforms and moats. Using these observations numerical models can be tested and developed accordingly.

1. Introduction

Ice streams and outlet glaciers discharge >90 % of ice from the interior of the Antarctic Ice Sheet to the oceans (Bamber et al., 2000). The fast ice flow of ice streams is mainly attributed to conditions and processes occurring at the ice stream bed (Clarke, 2005; Stokes et al., 2007). Current understanding of the subglacial environment is limited by its inaccessibility, which constrains accurate predictions of the stability of ice sheets (Morlighem et al., 2017). However, subglacial topography, such as bedforms, which form and evolve as a result of the interaction of ice flowing over subglacial material, can improve our understanding of subglacial processes.

Bedforms are abundant on ice stream beds (Dyke and Morris, 1988; King et al., 2016; Clark et al., 2018) and thus represent a key "geomorphological criterion" to identify the location and dynamics of palaeo ice streams (Stokes, 2018). The shape and elongation of streamlined bedforms have been linked to ice flow velocities (Hart, 1999; Stokes and Clark, 2002) and, combined with orientation, are used for the reconstruction of former ice flow and thermal regimes in the marine and terrestrial record. However, the processes involved in bedform formation have been debated since the early 19th century (Bryce, 1833), which resulted in numerous theories of bedform formation and evolution. Initially the basis of bedform formation theories was limited to observations in deglaciated terrain (e.g., Boulton, 1987; Clark, 1993; Hindmarsh, 1998; Shaw et al., 2000, 2008; Tulaczyk et al., 2001), where bedform geometry and properties represent the culmination of processes

---

* Corresponding author now at: Department for Geoscience, University of Tübingen, Germany.
E-mail addresses: Rebecca.schlegel@uni-tuebingen.de (R. Schlegel), aleisb@bas.ac.uk (A.M. Brisbourne), A.D.Booth@leeds.ac.uk (A.D. Booth), T.Murray@swansea.ac.uk (T. Murray), R.A.Clark@leeds.ac.uk (R.A. Clark).

https://doi.org/10.1016/j.geomorph.2024.109207
Received 22 June 2023; Received in revised form 4 April 2024; Accepted 11 April 2024

acting on the bedform during formation, glacier retreat and following exposure (Benn and Evans, 2011; Holschuh et al., 2020).

Effort has increased in recent years to map bedforms *in situ* beneath modern ice streams and glaciers using seismic and radar profiles (e.g., King et al., 2016; Bingham et al., 2017; Muto et al., 2019; Holschuh et al., 2020; Clyne et al., 2020). Initial imaging of subglacial bedforms beneath modern ice streams and glaciers comprised individual two-dimensional (2D) radar or seismic lines (e.g., Smith, 1997b; Smith and Murray, 2009; Finlayson et al., 2019). Using the radar reflectivity or seismic acoustic impedance of the bed, properties of the subglacial material have been determined (King et al., 2007; Muto et al., 2019; Clyne et al., 2020). Albeit often coarsely sampled, these datasets represent the best available images of *in situ* subglacial topography and properties (Holschuh et al., 2020).

Sparse 2D geophysical surveys are most appropriate for features that are aligned in some preferential direction, e.g. elongate bedforms parallel to ice flow. For more complex geometries (e.g., bedform terminations or features oblique to flow), 2D imaging is more problematic since reflected energy arriving from off-track features cannot be re-located to its true origin in a three-dimensional (3D) space. True 3D imaging and analysis of complex structures requires densely sampled survey grids and the application of 3D data processing approaches; acquisition of such data is labour intensive but compensated by improved image quality and greater insight into formation processes.

Here we present high-resolution radar data from a bedform and a moat beneath Rutford Ice Stream in West Antarctica. Previous radar studies on Rutford Ice Stream imaged basal topography including bedforms and moats with 500 m across-track sampling (King et al., 2009); however, owing to sparse sampling, detailed imaging was prevented. In the current study, we overcome the trade-off between across-track resolution and regional coverage (Holschuh et al., 2020) by combining a regional (relatively sparse) radar dataset with localized high-resolution radar grids that are compatible with 3D processing (e.g., Grasmueck et al., 2005). These data result in novel high-resolution images of a pronounced moat wrapped around the upstream end of a bedform. Additionally, we use seismic reflection profiles to constrain the composition of subglacial material. We conclude that the bedform consists of soft sediment with a relatively hard upstream end surrounded by a moat. We use these observations to interpret the subglacial conditions required for bedform initiation and assess theoretical models based on these.

1.1. *Bedforms in the palaeo record*

The term subglacial bedforms includes different bedforms, such as drumlins, mega-scale glacial lineations (MSGLs) and ribs or ribbed moraines (Rose, 1987). Drumlins are tear-drop shaped features of 100s—1000s m length (Menzies, 1979b; Clark et al., 2009), MSGLs (Clark, 1993) are elongated, parallel ridges of several 10s km length and ribs are ridges transverse to flow (Hättestrand and Kleman, 1999).

Studies in the palaeo record (e.g., Wellner et al., 2001; Ó Cofaigh et al., 2002; Margold et al., 2015) have highlighted that bedforms show a down-flow evolution; in the onset zone, bedforms are short and irregular, whereas further downstream the elongation ratio increases. Often this increase in elongation ratio is accompanied by a transition from a crystalline bedrock to a soft sedimentary basin (Wellner et al., 2001; Ó Cofaigh et al., 2002; Ottesen et al., 2008). This transition is assumed to be reflected in a change in flow dynamics, from basal sliding over a crystalline bed to faster movement by basal sediment deformation or ploughing over soft sediment (Ó Cofaigh et al., 2002).

The composition of bedforms in the palaeo record, specifically drumlins, are diverse (Stokes et al., 2011). Some drumlins mainly consist of bedrock (Raukas and Tavast, 1994; Evans, 1996; Heroy and Anderson, 2005; Kerr and Eyles, 2007), others have a bedrock core (Boyce and Eyles, 1991; Hart, 1997; Fuller and Murray, 2002) or consist mainly of sediment (Newman et al., 1990; Raukas and Tavast, 1994; Wysota, 1994; Hart, 1995a, 1995b, 1997; Rattas and Piotrowski, 2003). Drumlins consisting of sediment have been reported to be composed of homogeneous (Wright, 1973), sorted (Lemke, 1958; Zelčs and Dreimanis, 1997; Menzies and Brand, 2007) or stratified sediment (Dardis and McCabe, 1987; Hanvey, 1989). This variety of internal composition together with the large variability of bedform shapes (see overviews in Menzies (1979a); Patterson and Hooke (1995); Benn and Evans (2011)) has led to a variety of formation theories for drumlins.

1.2. *Bedforms beneath modern ice streams*

Recent studies of subglacial bedforms beneath modern ice streams were focused on Thwaites Glacier and Rutford Ice Stream (RIS, study area of this paper), both located in West Antarctica. The bedforms beneath RIS consist of short (~2 km) drumlins in the onset region of the ice stream (King et al., 2007) and longer (up to 14 km) features (King et al., 2009, 2016), referred to as MSGLs further downstream. The observation of the extension of a bedform over a seven-year period (Smith et al., 2007), measurements of seismic acoustic impedance, and radar reflectivity indicate that at least some bedforms beneath RIS are formed from soft sediment (Smith, 1997b; Smith et al., 2007; King et al., 2016; Schlegel et al., 2022). However, radar reflectivity and seismic acoustic impedance imply that the upstream end of some of these bedforms are harder (lower porosity) compared to the downstream tail (King et al., 2007; Schlegel et al., 2022). Beneath Thwaites Glacier, Holschuh et al. (2020) identified several bedforms based on radar surveys, including crag-and-tails, drumlins and MSGLs. Analysis of seismic acoustic impedance showed that these features are composed of soft till, with a steep stoss side, which is interpreted to consist of hard (presumed bedrock) material (Clyne et al., 2020; Alley et al., 2021).

1.3. *Theories of subglacial bedform initiation*

Theories of bedform formation typically concentrate on processes and conditions involved in bedform initiation, where three competing concepts can be distinguished: first, an initial topography with pre-existing topographic irregularities which act as a seed point for bedform growth or shaping; second, an initial flat topography but with inhomogeneities in the subglacial material; and third, an initial topography with no topographic or geologic irregularities (Boulton, 1987; Clark, 2011). Observations of a competent boulder or outcrop integrated into the stoss end of bedforms support the model of subglacial till deformation around pre-existing perturbations on the bed (e.g., Boulton, 1976; Clark, 1993). Ice flow over and around the perturbation creates a low-pressure zone in the lee of the perturbation which fills up with deforming sediment and thus extends the perturbation in the flow direction, creating an elongated bedform. This theory is consistent with several observations in the palaeo record (e.g., Hart, 1997; Hindmarsh, 1998; Clark, 2011) and beneath modern ice streams (King et al., 2009; Smith and Murray, 2009; Alley et al., 2021). However, some bedforms lack a boulder or outcrop at the stoss end (Patterson and Hooke, 1995; Stokes and Clark, 2001; Spagnolo et al., 2014) and motivate theories where formation occurs without a topographic seed point. Ice flowing over inhomogeneous subglacial sediment, such as a mosaic of stiffer and softer sediment patches (e.g. caused by variations in sediment permeability), can cause pressure variations at the ice-bed interface and thus the deposition of sediment (Boulton, 1987). This deposited material then acts as a topographic irregularity at the ice-bed interface and can further evolve into an elongated bedform. Other models anticipate the formation of bedforms without a topographic or geologic seed point by flow instabilities at the ice-bed interface (e.g., Hindmarsh, 1998; Menzies and Shilts, 2002; Fowler and Chapwanya, 2014). Over the last 25 years, different instabilities that invoke different dimensions and materials have been proposed. Early studies by Hindmarsh (1998) and Fowler (2000) model coupled flow between sediment and ice in two dimensions; Fowler (2010a) then introduces a thin water layer flowing between the ice and the sediment, which becomes unstable and produces rilling. Other approaches include spiral flows in the overriding basal ice (Schoof and Clarke, 2008), local pressure gradients (Barchyn et al., 2016), infilling of subglacial cavities (Fowler, 2009) as well as modelling of coupled ice-sediment flow in three dimensions (Fowler, 2010b; Chapwanya et al., 2011).

1.4. *Moats and theories of moat formation*

In the palaeo record, topographic over-deepenings or depressions, referred to as moats, are found in areas of previously fast-flowing ice. These features are often wrapped around the upstream end of bedforms, bedrock outcrops or ridges, and occasionally occur without an obvious obstacle (Dreimanis, 1993; Lowe and Anderson, 2002; Graham et al., 2009; Graham and Hogan, 2016). Beneath Thwaites Glacier, high-resolution radar data revealed moats around the stoss end of bedforms and bedrock outcrops (Holschuh et al., 2020; Alley et al., 2021). Similarly, radar data from RIS indicate moats around outcropping features and the upstream end of bedforms, as well as intervening troughs between bedforms (King et al., 2016).

Graham and Hogan (2016) stated that while a leading hypothesis of moat formation is lacking, theories include the erosion of material by localized water (Dreimanis, 1993; Lowe and Anderson, 2002), large flood events (Wingham et al., 2006), a slurry mix of sediment and water, or basal ice (Graham et al., 2009). Furthermore, Alley et al. (2021) stated that the pressure distribution of ice flowing against bedrock outcrops could be sufficient to enhance ice-till coupling upstream of the outcrops and erode material, which creates the observed moats. They further hypothesized that the eroded material could have been deposited in the lee of the outcrops, thus extending the bedform.

2. Rutford Ice Stream and data

RIS drains into the Ronne Ice Shelf, flowing with speeds of ∼380 m a^{-1} in the area of the grounding line (Murray et al., 2007). The area surveyed here lies 22 km upstream of the grounding line. The broad scale bed topography shows a central ridge bounded by two asymmetric valleys, up to 2.2 km deep (King et al., 2009). The bed includes numerous subglacial bedforms. Measurements of seismic acoustic impedance and radar reflectivity indicate that at least some bedforms beneath RIS are formed from soft sediment (Smith, 1997b; Smith et al., 2007; King et al., 2009; Schlegel et al., 2022). The observation of a bedform extending within a 7-year period, led to the conclusion that at least one bedform beneath RIS is a depositional feature (Smith et al., 2007).

Long-term flow stability (Gudmundsson, 2006; Murray et al., 2007; Vaughan et al., 2008) and the comprehensive geophysical survey history at RIS (e.g., Smith, 1997a, Smith, 1997b; Smith et al., 2007; King et al., 2009, 2016) make it an ideal location for mapping *in situ* subglacial bedforms and to investigate their initiation and evolution. Here we present a suite of different datasets and methods (Fig. 1) consisting of (1) data and methods that have been published previously, (2) new data that has been analyzed and processed with previously published methods and (3) new data that has been processed with a new method. Together these data cover the upstream part of a bedform (Fig. 2a), referred to as 'Smith Subglacial Ridge' or SSR (referred to as the 'Bump' in previous studies). The SSR is 13—50 m high and 100—360 m wide and at least 18 km long, although its downstream end has not been surveyed due to surface crevassing in the study area. Based on the elongation ratio of the SSR it was classified as a mega-scale glacial lineation (>18 km length, <550 m width (Clark, 1993; King et al., 2009)), although tapering ends and the significant high topographic relief were later used to classify it as a drumlin (King et al., 2016). We refrain from further discussion of the classification, considering that both types of bedform are part of a continuum (Stokes et al., 2013; Spagnolo et al., 2014; Ely et al., 2016).

Fig. 2b, c and d illustrate the coverage and sampling of the different datasets presented in this manuscript. The 500 m spaced radar lines of the Main grid (white lines in Fig. 2c) cover the SSR and the surroundings, while denser sampled radar data are focused on its upstream end and downstream area (black lines in Fig. 2c). Seismic reflection profiles were previously acquired along flow over the upstream end of the SSR and in the downstream area (Fig. 2b black dashed line). The geophysical data were jointly analyzed to obtain subglacial topography (Method I) and subglacial properties (Method II). The following list provides further detail on the radar and seismic datasets.

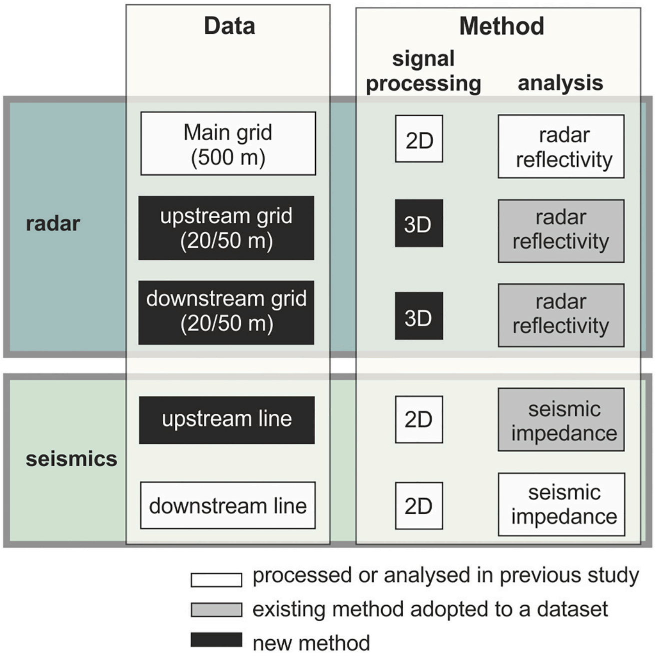

Fig. 1. Data and methods presented and analyzed within this study. Black boxes show new data and methods that have not been published previously. Grey boxes indicate existing methods applied to existing data and white boxes represent previously published data and/or methods.

2.1. *Radar data*

All radar data were collected across flow with 2 m along-track sampling (Fig. 2e) using a high frequency, ground based impulse radar system (DELORES, King et al., 2007). The difference between along- and across-track sampling is illustrated in Fig. 2e, where along-track sampling represents the sampling along the acquired (radar or seismic) line and across-track sampling the spacing between the acquired lines. Processing of radar data results in a vertical precision of 3 m (King, 2020). In total, three radar grids are described here:

(1) **Main grid** (white lines in Fig. 2c): previously published radar data acquired in 2016/17 (Schlegel et al., 2022), with 500 m across-track sampling (parallel to ice flow). As presented in Schlegel et al. (2022), the whole dataset covers a 15 × 17 km area. In this study, data is limited to a 3 × 17 km area. Based on this dataset, several regions of complex topography were identified and surveyed. Two of these are presented in this paper as follows:
(2) **Upstream grid, composed of two new radar datasets** (black lines in Fig. 2c) **DEL20UP and DEL50UP:** DEL20UP and DEL50UP were acquired in 2017/18 and 2016/17, respectively. DEL20UP covers a 1 × 3 km area with 20 m across-track sampling. DEL50UP utilizes 50 m across-track sampling, extending the DEL20UP coverage 2 km further downstream. Sampling in both grids is compatible with 3D migration. The Upstream grid is

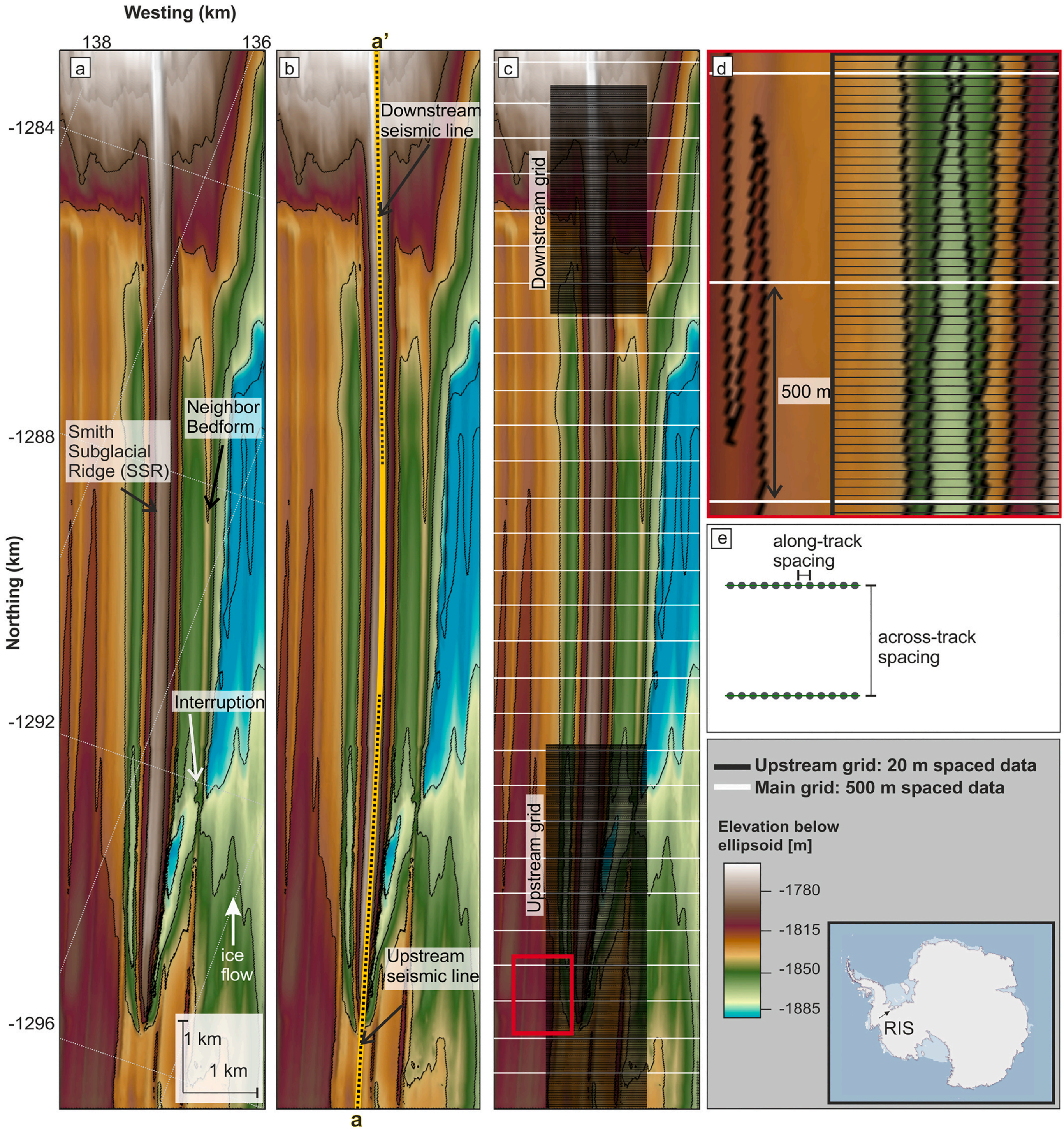

Fig. 2. Basal topography and bedforms beneath RIS. Elevation is relative to the WGS 84 ellipsoid and contoured at 20 m intervals. a) Topography (obtained by combining data in the Main, Downstream and Upstream grid) along the SSR. b) Topography with marked location of the Upstream and Downstream seismic reflection line, and profile a-a' shown in Fig. 7. c) Topography, coverage and sampling of data in the three radar datasets. The red box marks the inset shown in (d), illustrating the difference in across-track sampling between the 500 m spaced Main grid and the 20 m spaced data in the Upstream grid. e) Schematic illustrating across-track and along-track spacing. Map projection system is WGS 84 (EPSG:3031).

focusses on providing high-resolution imaging of the upstream extent of SSR.

(3) **Downstream grid** (black lines in Fig. 2c): new radar data covering a 1 × 3 km area with 20 m across-track spacing (other acquisition parameters as in DEL20UP). Data in the Downstream grid image the location of drill sites of the 2018/19 drilling campaign on RIS (Smith et al., 2021) as well as a downstream portion of the SSR.

2.2. *Seismic data:*

Upstream and **Downstream seismic lines** (black dashed line in Fig. 2b) are seismic reflection profiles acquired in 2009/10 and 2004/05

(F3 in Smith and Murray, 2009), respectively. Acquisition and processing of the Downstream seismic line are described in Smith et al. (2007) result in acoustic impedance values every ~120 m for both lines. Although not published in Smith et al. (2007), acquisition and processing of the Upstream seismic line are identical.

2.3. Method I: basal topography imaging

Most glaciological studies acquire, and therefore must process, ground-based radar data in a 2D manner (e.g., Murray et al., 2008; Church et al., 2018; Riverman et al., 2019). Even where multiple parallel 2D profiles are acquired, limiting the processing to 2D is often necessary, as the sparsity of sampling of the subsurface prevents 3D processing, specifically 3D migration. The key advantage of 3D migration is that energy reflected by off-track topography (e.g., flanks or bedform ends), which arrives at the surface oblique to the vertical, can be correctly relocated: the correct repositioning is impossible in 2D processing, which maps structures incorrectly into the along-track plane of the 2D profile.

In addition to correctly repositioning energy, migration improves the horizontal resolution of a profile in the direction in which it is applied. The horizontal resolution of data is initially dependent on the spatial sampling of the area, the frequency content and the processing of the data (Verdonck et al., 2015), and has a theoretical limit described by the first Fresnel zone (Yilmaz, 2001). On applying migration, horizontal resolution is reduced to one-quarter of a wavelength. Since 2D profiles can only be migrated in the plane of data acquisition, horizontal resolution is only improved in the along-track direction (Lindsey, 1989; Monk, 2010) and any out-of-plane energy will remain in the image as 'false' structure (French, 1974). 3D grids can be migrated in both along- and across-track directions, thus improving resolution in both directions and correctly reconstructing structure.

The different sampling of the Main grid (white lines) and the Upstream grid (black lines) is illustrated in Fig. 2d. Radar data in the Upstream and Downstream grid are compatible with 3D processing, but the across-track sampling of the Main grid is too coarse, and these data can only be processed in 2D. Only two seismic reflection profiles are available, thus processing of these is limited to a 2D space.

2.3.1. 2D radar and seismic data processing

Processing of the radar data in the Main grid are described in Schlegel et al. (2022) and consisted of assignment of acquisition geometry (assign traces to surface locations), bandpass filtering (passband 2—10 MHz), spherical divergence correction and 2D migration (using a finite difference approach and migration velocity of 0.168 m ns^{-1}) in ReflexW (Sandmeier Scientific Software). Processing of both seismic reflection lines is as described in Smith (1997b) and Smith et al. (2007) and includes topographic corrections, normal-moveout correction, surface-ghost deconvolution and 2D migration.

2.3.2. Spatial sampling requirements for 3D processing

For data to be compliant with 3D migration, the recorded reflected wavefield has to be non-aliased, meaning the along-track sampling interval has to be equal to or smaller than, the Nyquist sampling interval Δx_{max} (Grasmueck et al., 2005), defined as

$$\Delta x_{max} \leq \frac{v}{4 f_{max} sin(\beta_{max})}, \tag{1}$$

where f_{max} describes the maximum frequency, v the propagation velocity and β_{max} the maximum dip angle of the wave front.

Sampling along-track is dependent on the pulse repetition frequency, number of traces stacked and the speed at which the radar system is moving. To achieve dense sampling across-track when using a single antenna pair, several parallel, densely-spaced, radar lines can be acquired. Recent studies (e.g., Holschuh et al., 2020) have sampled the subsurface compliant with requirements of 3D migration by using multiple antennas on an airborne survey. However, to the best of our knowledge, no data compliant with 3D migration have been acquired using multiple coupled ground-based radar antennas in glaciological studies prior to this campaign.

2.3.3. 3D migration

The 3D processing strategy is similar to the 2D, including trace editing, 2—5 MHz bandpass filtering, and spherical divergence correction. Additionally, grid regularisation is performed (using interpolation in Mathworks MatlabR2021) to correct acquisition lines for GPS-tracked deviations away from parallel. The regularised grid has traces at 2 m spacing along-track, and 20 m and 50 m across-track. 3D Kirchhoff time migration was applied in Landmark SeisSpace/ProMAX, with a migration aperture limited by a maximum dip angle (Upstream grid: 45^0, Downstream grid: 30^0) and stretch mute (Upstream grid: 30 %, Downstream grid: 15 %). Migration-induced noise (Robein, 2010; Jones, 2014) was suppressed by applying a 2—5 MHz bandpass filter, encapsulating the radiated signal bandwidth. This processing resulted in a theoretical horizontal resolution of 24 m in both along- and across-track directions. For comparison to a 2D processing strategy, the theoretical resolution of the Main grid is 24 m along-track and 500 m across-track.

2.3.4. DEM generation and analysis

The bed reflection in all radar datasets was picked on the first coherent arrival around the expected two-way traveltime of 25,000 ns for the 2100 m ice thickness (Figs. 3, 4). In areas where 2D and 3D migrated radar data overlap, only the 3D migrated bed reflection was picked. The bed reflection traveltime in both the 2D and 3D radar data were then interpolated on a surface with a 20 × 65 m cell size.

We determined the edge of topographic features by manually mapping abrupt topographic changes along the bed. To highlight small-scale features and therefore enhance the efficiency and accuracy of interpolation (Zhao et al., 2016) we calculated the dip and dip azimuth of the dip for the Downstream and Upstream grids. The dip and the dip azimuth of the dip of the bed topography describes the deviation of the bed topography from a horizontal plane. The angle between the bed topography and the horizontal is given as the dip. The direction towards which the bed topography is dipping (e.g., relative to the ice flow direction) is called the dip azimuth of the dip.

To analyze the volumes of the features relative to each other, such as bedforms and moats, the volumetric difference of the features relative to a reference surface is calculated. The reference surface is based on the DEM shown in Fig. 2a, filtered to omit the short wavelength features of the bed topography. Subtraction of the DEM from the reference surface allows the calculation of the volume of features above and below the reference surface.

2.4. Method II: basal properties

We estimate sediment porosities from radar amplitudes following the procedure outlined in Schlegel et al. (2022) and seismic acoustic impedance following Smith, 1997b and Smith et al. (2007).

2.4.1. Subglacial properties from seismic data

Acoustic impedance, the product of acoustic seismic velocity and density, is a commonly used tool to assess subglacial material and differentiate between soft deforming or dilated, and stiff non-deforming sediments (e.g., Atre and Bentley, 1993). The strength of the bed reflection is used to estimate the acoustic impedance of the bed material at the ice base. For the seismic profiles in this study, the primary bed reflection strength was calibrated using the surface to bed multiple reflection. This method accounts for englacial attenuation and is used to determine the basal reflection coefficient. The measured basal reflection coefficient is then used to derive the acoustic impedance of the basal material by assuming an acoustic impedance of basal ice (3.33 × 10^6 kg m^{-2} s^{-1}; Smith, 1997b and Smith et al. (2007)).

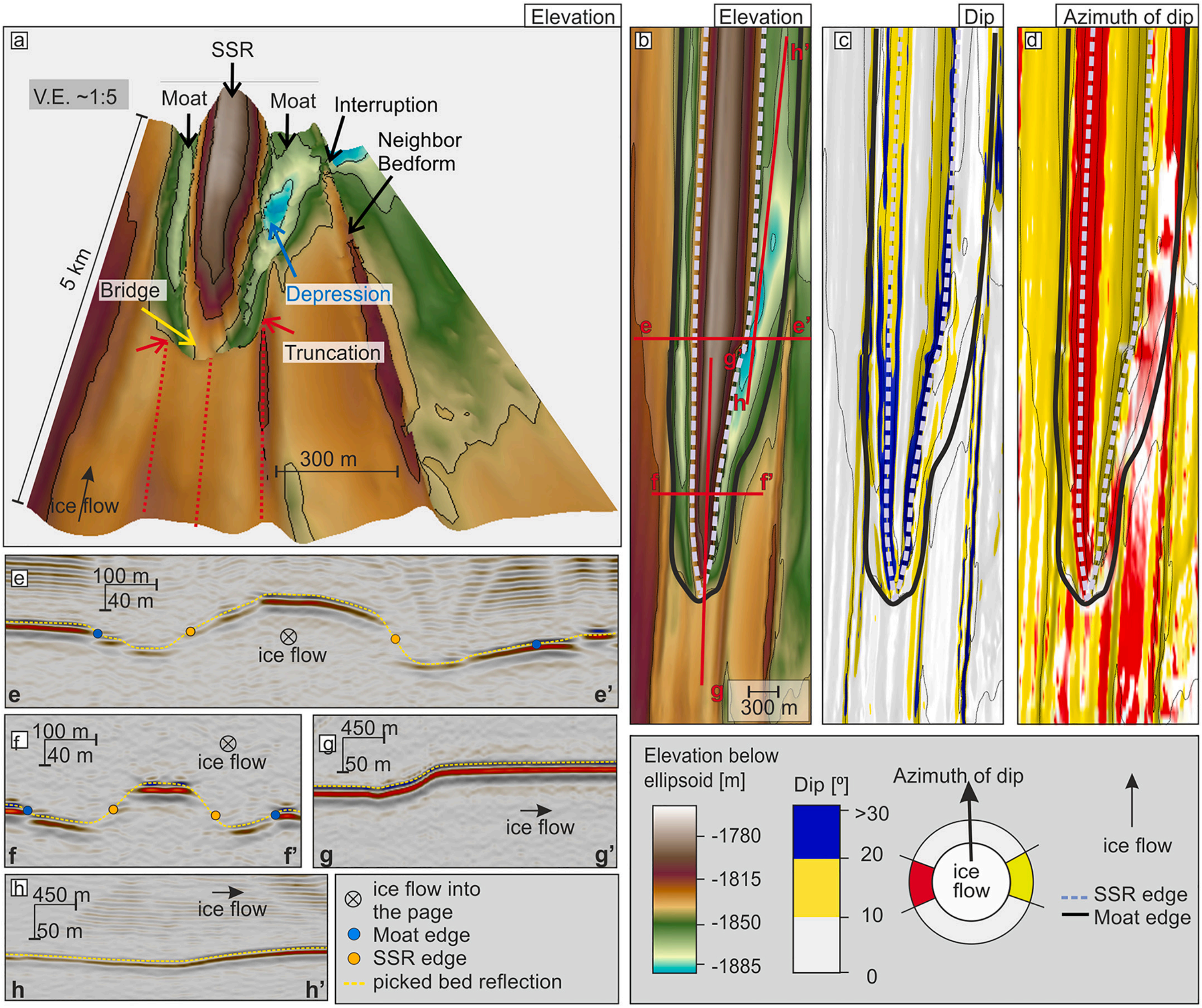

Fig. 3. Bed topography and radargrams of data in the Upstream grid. a) Bed elevation (relative to the WGS 84 ellipsoid and 20 m contour intervals) in perspective 3D view, b) bed elevation in plan view, c) dip and d) azimuth of the dip of the bed topography in plan view. The white dashed and black solid line mark the outline of the SSR and the moat, respectively. Colour schemes for the different attributes are given in the legend. 3D migrated radar data along a profile e) across the SSR approximately 2.5 km downstream of its stoss face, f) across the upstream end of the SSR, g) across the upstream end of the SSR and h) along the deep moat. See red lines in (b) for the location of the radargrams. Vertical and horizontal scaling of the radar profiles along and across flow was adapted for illustrative purposes.

Values of acoustic impedance measured at the bed in the range 2.2—3.8 × 10^6 kg m^{-2} s^{-1} are attributed to till, following Atre and Bentley (1993). However, this range should be thought of as a continuum. High porosity dilated tills lie at the lower end, with dilation being a result of deformation. We refer to materials in the middle of this range as lodged till, having lower porosity than the dilated till. Materials with values at the upper end of this range are referred to as stiff till (Atre and Bentley, 1993; Brisbourne et al., 2017; Muto et al., 2019; Clyne et al., 2020). As this acoustic impedance range straddles that of ice, a polarity reversal at the bed reflection is observed for the dilated till with low acoustic impedance. No polarity reversal is observed for stiff till. This polarity reversal provides a reliable bulk discriminator for the end members of these materials. As the acoustic impedance values of lodged till are close to that of ice, only a weak reflection may be observed. This has led some authors to use a binary nomenclature of 'hard' and 'soft' beds (Muto et al., 2019).

2.4.2. *Subglacial properties from radar data*

During acquisition, the traveltime of radar arrivals is recorded as well as the voltage (also termed 'amplitude') of the signals received. Bed properties can be inferred from the amplitude of reflections, with greater electromagnetic contrast associated with stronger reflected amplitudes (e.g., Gades et al., 2000; Catania et al., 2003; Murray et al., 2008; Ashmore and Bingham, 2014). The analysis of the amplitude in the Main grid has been described in Schlegel et al. (2022), and the same approach is applied here for the Upstream and Downstream grids. Prior to migration, all radar data have been corrected for geometric spreading and englacial attenuation losses (depth averaged attenuation rate in this area according to Schlegel et al. (2022) corresponding to ~20 dB/km), and for consistency with Schlegel et al. (2022), the same finite-difference 2D migration scheme is applied. We calculated the received power of the bed reflection following Gades et al. (2000), by summing the square of the amplitudes within a 280 ns window centered around the bed reflection (Schlegel et al., 2022). Analysis of Main grid data

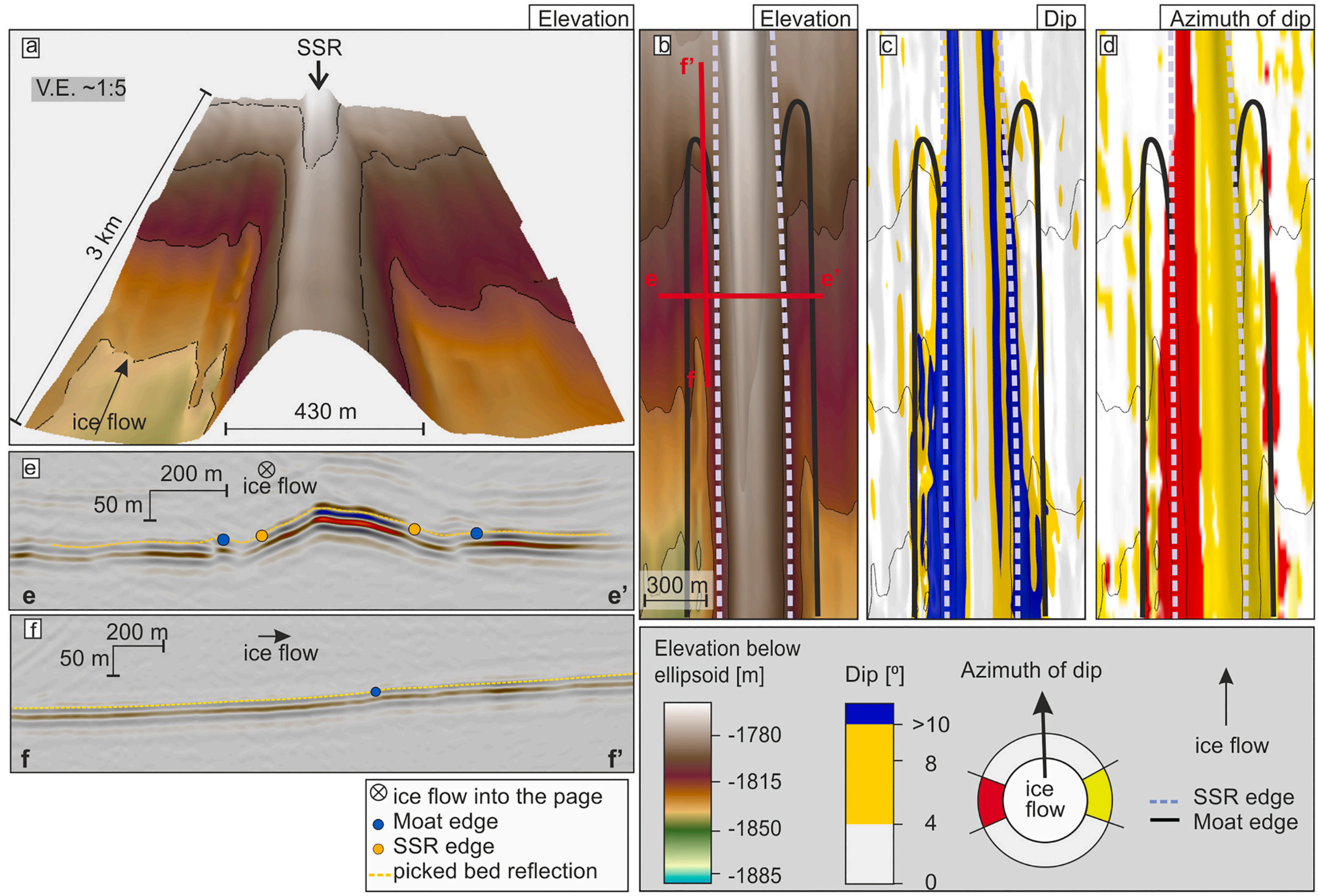

Fig. 4. Bed topography and radargrams of data in the Downstream grid. a) Bed elevation (relative to the WGS 84 ellipsoid and 20 m contour intervals) in perspective 3D view, b) bed elevation in plan view, c) dip and d) azimuth of the dip of the bed topography in plan view. The white dashed and solid black line mark the outline of the SSR and the moat, respectively. Colour schemes for the different attributes are given in the legend. e) 3D migrated radar profiles across the downstream part of the SSR, f) 3D migrated radargram along the shallow moat. See red lines in (b) for location of radargrams.

(Schlegel et al., 2022) has shown that sensitivity of the wavelet to roughness on the bed in this area is small. Within this paper, we refer to the square root of the received power, which represents the voltage corrected for ice thickness variations as bed-reflection voltage (BRV). The BRV is proportional to the reflection coefficient R, but the BRV only represents relative values and cannot be linked to the absolute bed properties and porosities without further calibration. The BRV was calibrated using a theoretical reflection coefficient calculated using parameters identified along a seismic line within the Main grid as presented in Schlegel et al. (2022). The bed in the reference area is assumed to consist of a 40—50 % porous sediment, with a matrix consisting of sand with relative dielectric permittivity of 3—6, and solely water in the pore space. This results in a bulk relative dielectric permittivity of 21—32, and together with the assumption that the overlaying medium consists of ice, a reflection coefficient of 0.6—1.8. We refer to the calibrated BRV as reflectivity, which is unitless. Assuming (1) uniform ice properties over the area (as assumed when correcting for attenuation), (2) the subglacial sediment consists of a sandy matrix with relative dielectric permittivity of 3—6 (representing the range of dry sands) and (3) the pore space in the sediment to be saturated with water (no air in the pore space), the variations in reflectivity can be assigned to variations in porosity. Following this approach, reflectivity values of 0.6—1.8 are assigned to sediment with 30—50 % porosity. Lower reflectivity is taken to indicate a lower porosity and vice versa. Following the approach used for the seismic acoustic impedance, we assume sediment porosities in the range 30—50 % (grey box in Fig. 7b) to represent dilated (deforming) sediment. Sediment with lower porosities is assumed to be stiff and non-deforming.

3. Results

3.1. Bedform and moat topography

Bed topography derived from combining 3D and 2D migrated data is illustrated in Fig. 2a and shows the SSR with a depression, referred to as the 'moat', surrounding the upstream end. Figs. 3 and 4 show detail of the topography (panel a, b) as well as radargrams (e—h/f), of the Upstream and Downstream grids respectively. The SSR is characterized by a sharp topographic rise at the stoss face (25 m elevation change over 25 m) and steeply dipping (partly over 30°) flanks on either side of the SSR (Fig. 3 a, c, f). The steepness of the flanks results in weak and discontinuous reflections at the upstream end (Fig. 3 f). The flank steepness decreases downstream (Fig. 3c vs. Fig. 4c), resulting in continuous reflections downstream (Fig. 4e).

The edges of the SSR and moat in the Upstream grid are visible in the elevation map (Fig. 3a, b), whereas in the Downstream grid, where topography is less abrupt, the moat edges can only be identified using the dip and dip azimuth of the dip (Fig. 4c, d). The moat surrounds the upstream part of the SSR. However, a 'bridge' upstream of the stoss face (Fig. 2a, 3a) interrupts the moat. This bridge is around 150 m long

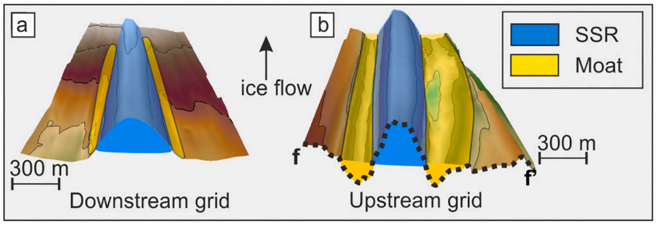

Fig. 5. Comparison of the size and volume of the moat (yellow) and SSR (blue) in the Downstream (a) and Upstream (b) grids. (b) shows a part of the Upstream grid, for the location of crossline f-f' see Fig. 3b.

(along flow) and 80 m wide. The reflection along the bridge is clearly visible (Fig. 3g). On either side of the bridge the topography deepens in the downstream direction. The moat truncates smaller streamlined bedforms (80—130 m width, 4—17 m height; red dashed line, Fig. 3a). Furthermore, the 'neighbor' bedform, between the depression and a deeper bed area, appears to be disrupted (Fig. 2a, 3a), where the bedform height drops and then rises again. The moat in the Downstream grid is visible as a slight depression, about 150 m wide and up to 10 m deep, on either side of the SSR (Fig. 4 a—d).

3.1.1. Size of moat and bedform

Crest-to-moat elevation around the upstream part of the SSR ranges from 35 m at the stoss end to 100 m around 2.5 km further downstream

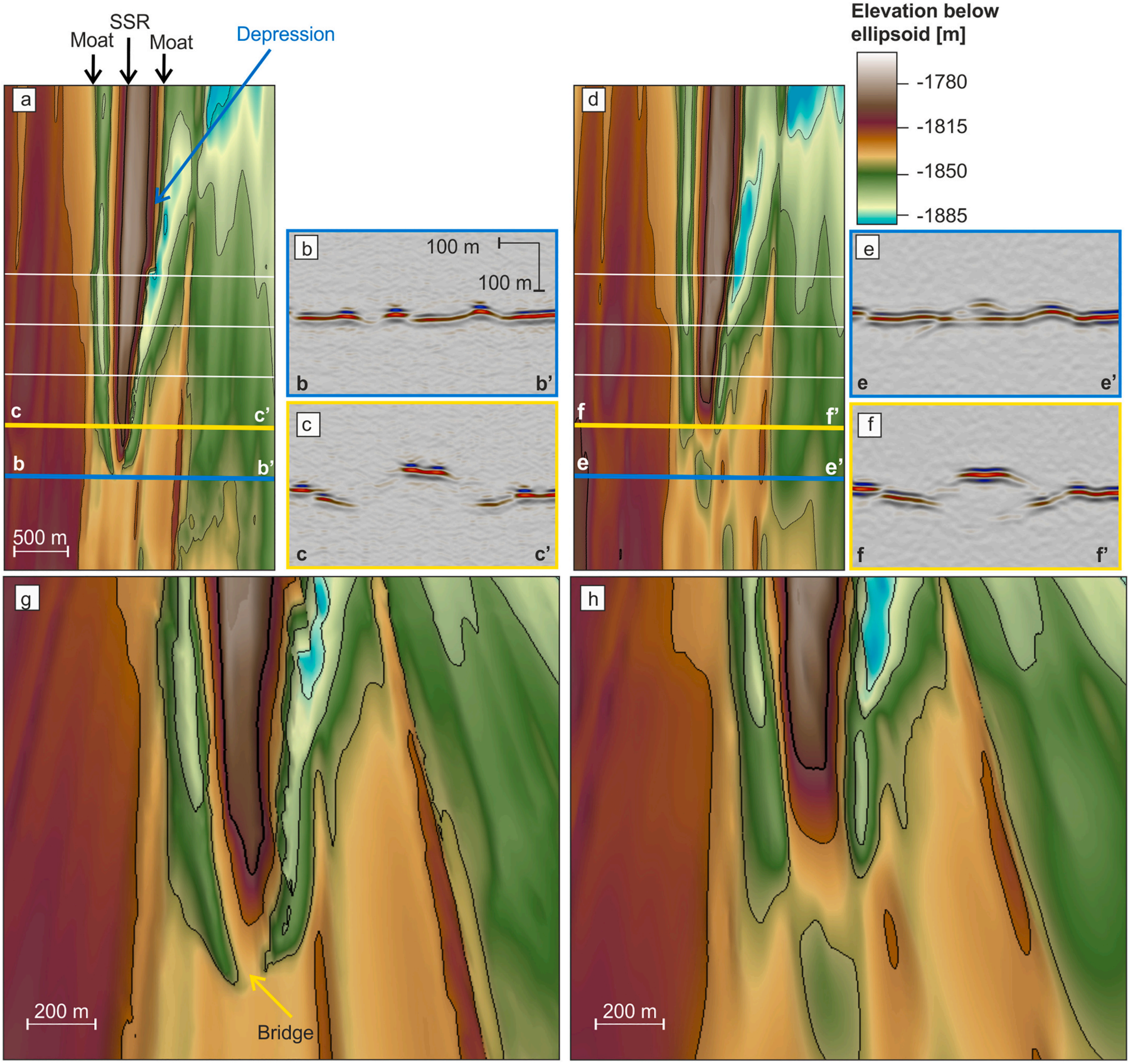

Fig. 6. Comparison of basal topography of the upstream end of the SSR in the Upstream grid (a, b, c, g) and the Main grid data (d, e, f, h). a) and g) show the bed elevation based on the Upstream grid data. d) and h) show the bed elevation based on Main grid data. b) radargram of the data upstream of the SSR for the Upstream grid and e) the Main grid, respectively. c) radargram of the data along a line crossing the SSR in the Upstream grid and f) in the Main grid, respectively. Location of data shown in the radargram relative to the bed elevation are marked by the blue and yellow lines in a and d, respectively.

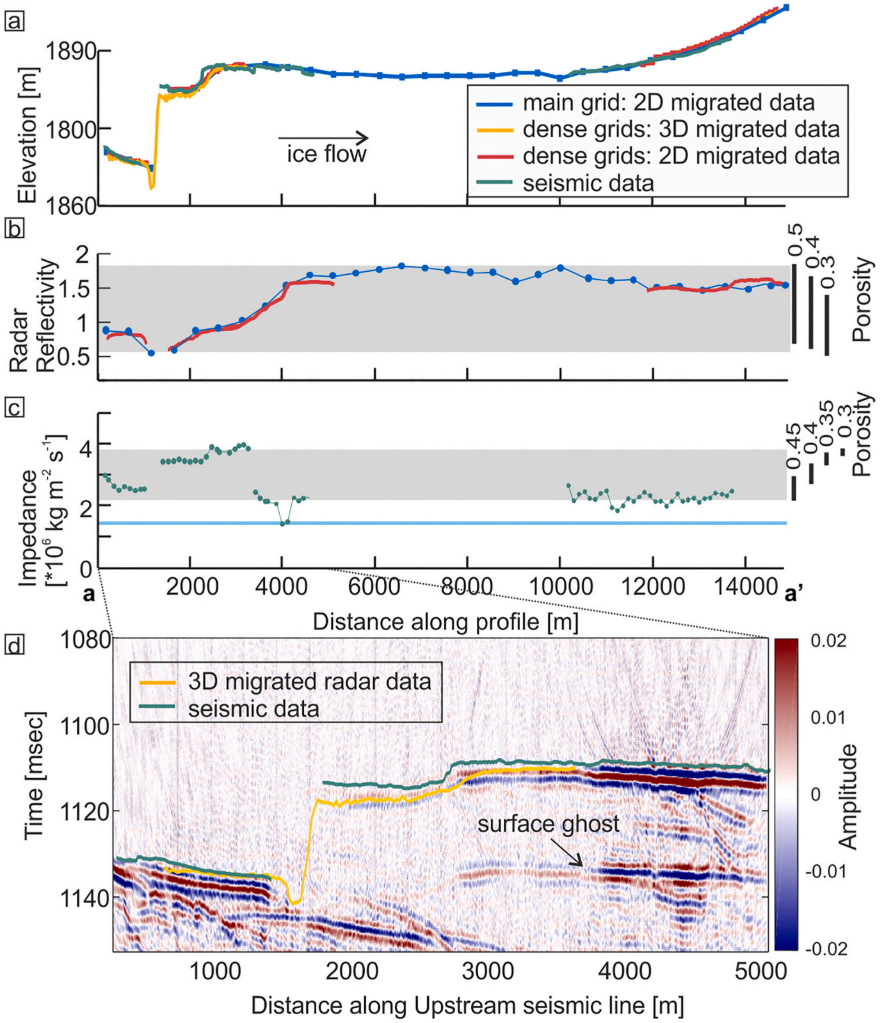

Fig. 7. Properties along the SSR's crest (a—a' in Fig. 2b). a) Topography along flow from 3D and 2D radar and seismic data, b) radar reflectivity from 2D migrated radar data. Porosity ranges as in Schlegel et al. (2022). c) Acoustic impedance of the bed reflection. No data is available between 5—10 km. Porosity ranges as in Smith and Murray (2009). d) Seismic profile along the SSR, including the pick of the first coherent arrivals (green) and the corresponding topography (yellow) from 3D radar data. Conversion of radar two-way traveltime to corresponding seismic two-way traveltime was calculated by accounting for a firn thickness of about 100 m and an electromagnetic wave velocity of 0.168 m ns^{-1} and acoustic wave velocity of 3742 m s^{-1}. Gaps in the topography, reflectivity and acoustic impedance represent areas of complex reflection in 2D seismic and 2D radar data over the steep stoss end. Grey shaded areas in b and c mark porosity range (30—50 %) associated with deforming sediment.

(Fig. 3e, f). Similar to that described in King et al. (2016), the crest rises steeply to a maximum, and then tapers slowly in the downstream direction. The moat on either side of the SSR reaches maximum depth adjacent to the highest point of the SSR. The right-hand moat contains an additional depression (~180 m wide, 1100 m long, maximum 9 m deep compared to the contour line surrounding the blue colored area), where the moat reaches its maximum depth (~55 m beneath mean level of the topography upstream of the moat, Fig. 3a, b), ~2.5 km downstream of the stoss face of the SSR. The width of the left-hand moat appears relatively constant, at around 200—250 m, while the right-hand moat widens further downstream (up to 350 m).

Omitting the short wavelength features of the bed topography, we estimate the volume of the moat and the SSR (Fig. 5). In the Upstream grid, both volumes are of similar scale (around 4.7 × 10^7 m^3), whereas the moat volume (1.8 × 10^6 m^3) is an order of magnitude less than the SSR (2.4 × 10^7 m^3) in the Downstream grid. This relationship is also applicable when comparing the moat depth and the SSR height.

3.2. 2D VS. 3D migration

Fig. 6 shows the comparison of topography (a, d, g, h) and radargrams (b, c, e, f) of the Main grid and the Upstream grid. Naturally, data across 500 m spaced radar lines sample the subsurface much more coarsely, which limits the across-track resolution. However, comparing the radargrams of both datasets acquired upstream of the SSR (Fig. 6b, e) shows additional energy arrivals visible prior to the bed reflection in the Main grid data, compared to the Upstream grid data. Further downstream, both radargrams (Fig. 6c, f) show similar topography. However, data in the Main grid contain dipping reflections on either side of the SSR, which are lacking in the Upstream grid data. In plan view, topography based on both datasets image a moat on either side of the SSR. A difference between the topography from both datasets is visible around the upstream end of the SSR. The Main grid implies the existence of a depression upstream of the SSR, lacks the bridge, and shows the SSR to be shifted downstream, compared to the Upstream grid.

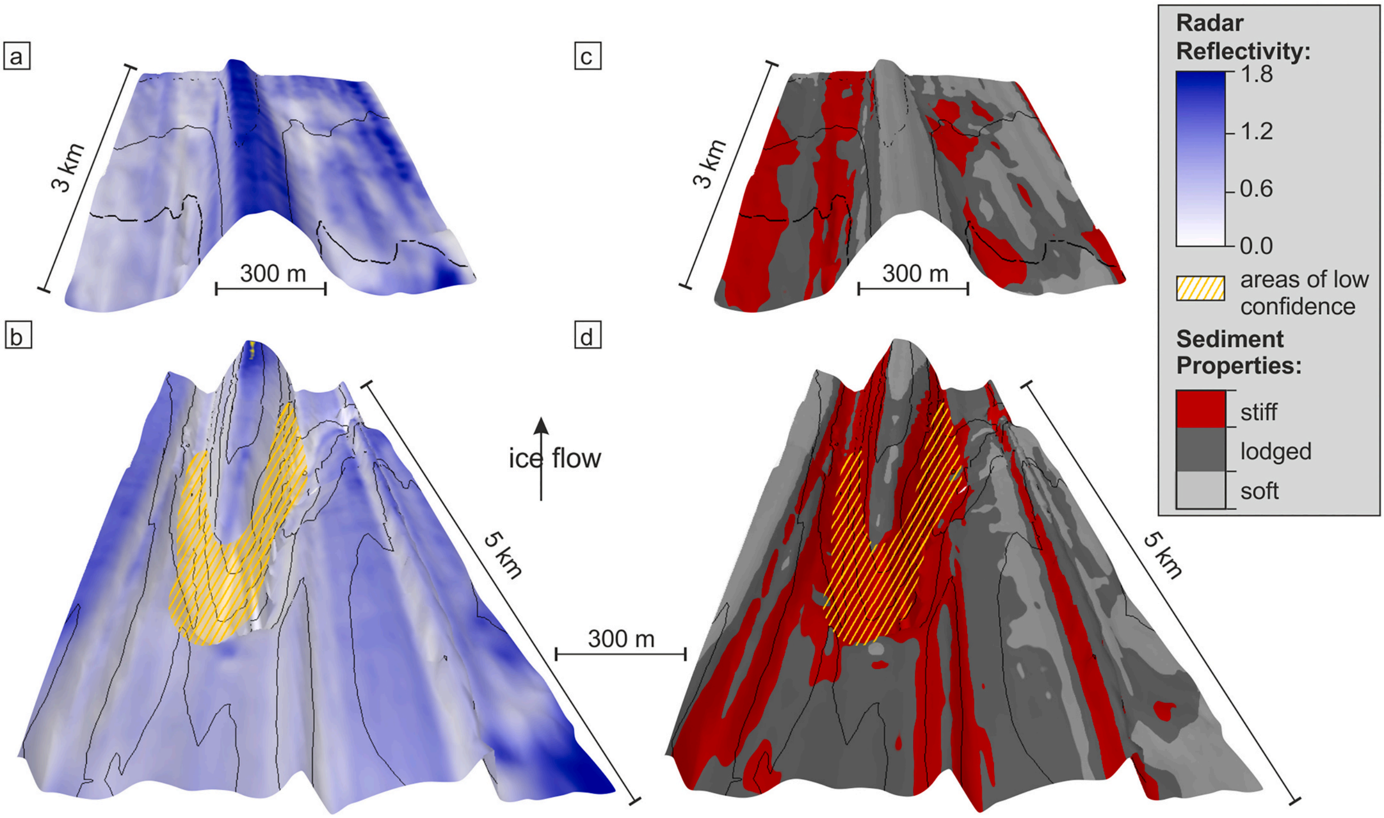

Fig. 8. Bed reflectivity and interpreted properties from 2D processed radar. a) Radar reflectivity from 2D migrated data in the Downstream and b) Upstream grid. Areas with incoherent and discontinuous bed reflections are hatched in yellow. c) Interpreted sediment properties based on radar reflectivity in the downstream and d) upstream grid. Reflectivity related to sediment porosity below 30 % are categorized as stiff sediment. We sub-categorize the range of porosities associated with deformation in lodged sediment, for the lower part of the porosities (30—40 %) and deforming sediment for the upper porosities (40—50 %).

3.3. Subglacial properties

Fig. 7 illustrates the topography and properties calculated along a profile, starting upstream of the SSR and then following the crest of the SSR (see Fig. 2a for the location of the line). Fig. 7a shows the basal topography from the different radar and seismic datasets. The topography in the different datasets is in good agreement, however the 2D migrated seismic and radar data lack signal from the stoss face of the SSR. Radar reflectivity from the Main grid (blue dots and line) and the 2D migrated Upstream and Downstream grid (red line) are shown in Fig. 7b. Acoustic impedance values calculated along the seismic reflection profiles are shown in Fig. 7c. For both the reflectivity and the acoustic impedance, the corresponding porosity ranges are displayed using vertical bars on the right-hand side of the plot. Due to the uncertainties of the calculation of porosities, specifically based on the radar reflectivity, individual bars are overlapping. The grey bar in the background indicate the porosity ranges associated with deforming sediment (30—50 %). Fig. 7d shows the seismic reflection profile along the SSR, including the pick of the first coherent seismic arrivals (green) as well as the corresponding topography from 3D radar data (yellow) from the Upstream grid. As described above, 3D migrated radar data image the topography along the whole line, but 2D migrated seismic data are lacking a coherent reflection from the steep stoss face. Apart from the surface ghost, few seismic reflections are visible within the SSR (Fig. 7d).

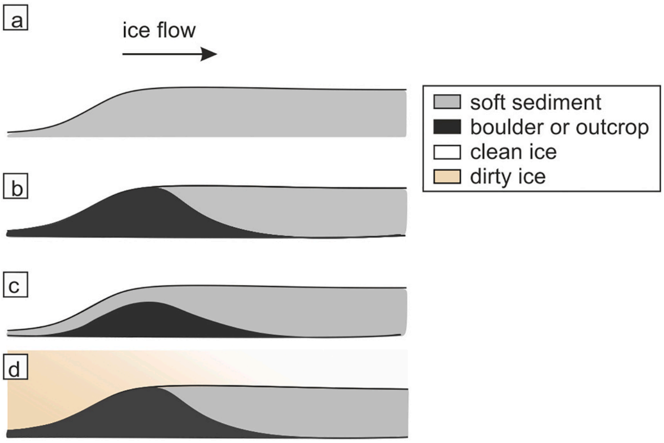

Fig. 9. Schematic of bedform composition: a) bedform composed of soft sediment, b) boulder or outcrop incorporated at the end, c) incorporated boulder or outcrop at the upstream end overlain by soft sediment, d) bedform composed of a boulder or outcrop at the upstream end with debris incorporated into the basal ice above the bedform.

Upstream and around the SSR, radar reflectivity is low (<1) when compared to the SSR crest (<2). Once the stoss face is approached, the radar reflectivity continually increases along the crest until approximately 2.5 km downstream of the stoss face, where the reflectivity remains between 1.5 and 1.7 for several kilometers (Fig. 7b). Reflectivity values along the profile from the Main grid and the dense radar grids are in good agreement (Fig. 7b). Acoustic impedance increases abruptly (from 2.5×10^6 to 3.5×10^6 kg m^{-2} s^{-1}) at the location of the stoss face of the SSR and remains high until 2.3 km downstream of the stoss (Fig. 7c at ~3800 m distance), where impedance values are as low as 1.5×10^6 kg m^{-2} s^{-1}. Acoustic impedance values in the downstream seismic line are relatively constant at around 2×10^6 kg m^{-2} s^{-1}, with no abrupt changes.

Radar reflectivity from the 2D migrated data is shown in Figs. 8a and b along the extent of the Downstream and Upstream grids. Reliable identification of properties in some areas is limited by discontinuities in the radar reflection (Fig. 3e, f), which is attributed to the complex geometry. Therefore, we refrain from interpreting radar reflectivity in these areas (yellow hatching in Fig. 8b). Reflectivity is high (above 1.7) along the whole width of the SSR crest in the Downstream grid. The SSR flanks show lower reflectivity (0.6—1). The moat and the flanks around the upstream end of the SSR cannot be imaged with continuous reflections. Where reflections are continuous in the Upstream grid, most of the moat is of low reflectivity. In the Downstream grid, the reflectivity in the moat has patches of higher and lower reflectivity. The crest of bedforms upstream of the moat show reflectivity of 0.6, with decreased reflectivity along the flanks of these small bedforms.

4. Discussion

4.1. Bedform and moat size and composition

Because of its significant height and width, specifically at the upstream end, the SSR is a very prominent feature on the bed of the RIS. The abrupt topography at the upstream end is further amplified by the dimensions of the moat that is surrounding the SSR. The depth of the moat on either side of the SSR scales with the height of the SSR, which is reflected in the volumes of either feature. Further along flow, the moat depth and SSR elevation decrease, resulting in less abrupt topography, which can, however, be resolved in radar data. The SSR is clearly visible in the Downstream grid, where the moat is very shallow (<10 m depth). We interpret this subtle depression in the Downstream grid to be the downstream expression of the moat (black line in Fig. 4b). The moat does not terminate at the same distance along either side of the SSR; the right-hand moat appears to be 150 m longer. Assuming that the moat is continuous between the Upstream and Downstream grids, the moat length is ~10.5 km.

4.1.1. SSR composition

Across the entire crest of the SSR, radar reflectivity values at the bed are consistent with deforming sediment of 30—50 % porosity. Values of seismic acoustic impedance lie almost entirely in the range of deforming sediment, with some areas (3—3.5 km) of slightly higher acoustic impedance, just outside the range of what is considered to represent deforming sediment. Some values of acoustic impedance indicate dilated sediment at up to 45 % porosity (4 km and from 10 km onwards). Comparing the upstream end and downstream part of the SSR, the topographic differences observed may by correlated to the observed changes in radar reflectivity (Fig. 7b), as well as seismic acoustic impedance (Fig. 7c), implying different sediment properties present at the ice-bed interface along flow. Radar reflectivity increases along flow, implying that the porosity increases. Acoustic impedance is relatively high at the upstream end and reduces approximately 2.3 km downstream of the bedform's stoss end (Fig. 7c), implying a harder upstream end with softer material downstream. Both these observations can be interpreted to reflect an increase in sediment porosity along flow which would causes the material to soften.

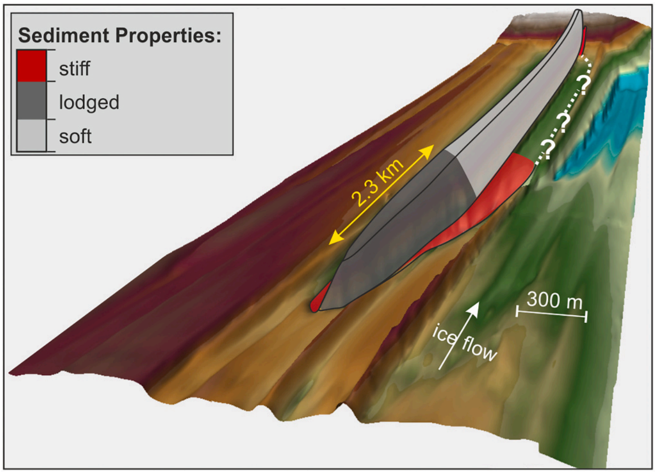

Fig. 10. Interpretation of bedform composition. Missing tracks of the outline of the moat between the Downstream and Upstream grid are marked by question marks.

A harder upstream end along with softening of sediment along flow is consistent with observations of other bedforms beneath RIS (King et al., 2007; Schlegel et al., 2022). As the composition of the upstream end of bedforms is a key element of bedform initiation theories (Clark, 2011), we evaluate potential compositions of the upstream end based on the observations from seismic and radar measurements in more detail. Fig. 9 illustrates theoretical bedform compositions considered here. These include, (a) a bedform entirely composed of soft sediment, (b) a bedform composed of a boulder or outcrop incorporated at the upstream end acting as a seed point for bedform and/or moat initiation (Stokes et al., 2011; Alley et al., 2021) and soft sediment downstream, (c) as in (b) but the boulder or outcrop at the upstream end is draped with soft sediment and (d) bedform composition as in (b), but debris is incorporated into the ice (referred to as dirty ice) above the upstream end of the landform, whereas options (a)—(c) consider the ice to be 'clean'.

To describe the composition of the bedform, we rely on radar and seismic data. Radar energy is less likely to penetrate deep into the subglacial material, and thus only represents properties at the ice-bed interface. Seismic energy will penetrate through the subglacial material, as demonstrated in previous studies on the RIS where deeper (over 100 s m deep) sub-bed reflections are present (e.g., Smith, 1997a,b; King et al., 2007; Smith and Murray, 2009). Thus, we expect seismic energy to penetrate through the whole depth of the SSR and further into the subglacial material. This would allow us to differentiate between material boundaries within the SSR.

4.1.1.1. Boulder or outcrop at the upstream end. If present, we would expect an incorporated boulder or outcrop (Fig. 9b) with dimensions of the stoss end of the SSR to be composed of a competent material in order to withstand the erosive forces in such a terrain (fast-flowing ice velocity, high erosion rates (Smith et al., 2007)). Acoustic impedance values at the upstream end (Fig. 7c distance 1400—3900 m) lie at the upper end of the porosity range of deforming sediment (30—50 %), with some values above, excluding any material except sediment or poorly lithified sedimentary rock at the ice-bed interface.

Subglacial sediment samples retrieved from drilling on ice streams are rare and to our knowledge limited to unlithified sediment. We therefore can only draw conclusions on potential porosity ranges in sedimentary rock from studies outside of the field of glaciology, such as Ó Cofaigh et al. (2007) and Klages et al. (2020) who reported marine sedimentary rock with porosities up to 40 %, which is in the range of porosity calculated for the SSR upstream end. However, we would expect to resolve stratigraphy within a 100 m thick marine sedimentary rock (e.g., Gawthorpe et al., 2022), as well as dipping reflections from the downstream end of a sedimentary outcrop in the seismic data. We therefore conclude that acoustic impedance values give no indications that the upstream end is composed of a sedimentary outcrop or boulder. Nevertheless, in the following we will explore possible reasons for a lack of high acoustic impedance values by considering interference effects caused by a boulder or outcrop overlain by sediment (Fig. 9c) or overlain by debris-bearing ice (Fig. 9d).

4.1.1.2. Smaller boulder or outcrop overlain by sediment. A boulder or outcrop overlain with soft sediment presents a high acoustic impedance contrast (e.g., Muto et al., 2019; Clyne et al., 2020). Therefore, we would expect to see a strong seismic reflection within the SSR if such a feature were present; seismic reflections from within the SSR are absent in our data. The absence of reflections within the SSR (Fig. 7d) does not immediately preclude the existence of a boulder or outcrop. Energy reflected from a boulder or outcrop overlain by a thin sediment layer might destructively interfere, resulting in a weak or absent reflection and an inferred low acoustic impedance contrast. In such a scenario, the thickness of the sediment layer is limited to 2.2—3.3 m ($\lambda/6$—$\lambda/4$; Booth et al., 2012). If the sediment layer thickness deviates beyond this narrow range, a significant change in reflection strength would result. Sediment layer thickness would increase at the downstream end of a boulder or outcrop (Fig. 9c), resulting in a significant change in reflectivity, which is not observed here.

4.1.1.3. Boulder or outcrop overlain by debris-bearing ice. In addition to interference effects from the subglacial material, acoustic impedance might be altered by debris incorporated into the basal ice (Fig. 9d). The acoustic impedance of the ice-bed interface is calculated, assuming the upper material to be clean ice. The incorporation of debris into the basal ice affects the seismic velocity and density of the basal ice, thus the acoustic impedance. Neglecting the effects of debris-bearing ice could cause calculated values for the basal sediment to be too low. Muto et al. (2019) calculated the effect of debris-bearing basal ice on the calculated acoustic impedance and found that a basal ice layer containing 5 % of sediment would increase the impedance by ~10 %. Images of borehole cameras and results from drilling on Antarctic ice streams indicate spatial variability of entrained debris into the basal ice (Christoffersen et al., 2010; Smith et al., 2021). In the area studied here, we do not have information about the quantity of debris in the basal ice (Smith et al., 2021). However, from unpublished drilling results, we expect only relatively small changes in englacial debris within this area. In that case, the increase in acoustic impedance for basal ice with for instance 5 % of sediment is negligible, as it is not sufficient to increase the acoustic impedance to a value that can be considered originating from a boulder or outcrop.

For reasons stated above, we exclude the presence of a boulder or outcrop at the upstream end of the SSR. We interpret the whole SSR to be composed of sediment (Fig. 9a) with porosities between 30 and 50 %. To better differentiate between the sediment that forms the harder upstream end and the softer downstream part of the SSR, we use the terms 'lodged' for sediment that has a decreased porosity (30—40 %) and 'soft' for sediment with a high porosity (40—50 %). Following this, we describe the sediment at the upstream end as lodged, being of lower porosity than downstream (Fig. 10).

Variations in sediment stiffness within bedforms are attributed to different till origins (Goldstein, 1994; Hart, 1995a), spatial variations in drainage efficiency of the substratum (Rattas and Piotrowski, 2003), or temporal variations in subglacial water pressure causing over-consolidation (Craig, 2004; Ives and Iverson, 2019). Furthermore, ice flow against an obstacle can create a high-pressure zone at the stoss end (Alley et al., 2021) resulting in dewatering and enhanced consolidation. The similarity of the current ice thickness (2.1 km) and the length-scale of the lodged sediment (2.3 km, yellow arrow in Fig. 10) highlights a potential scale dependence of the length of consolidation and ice thickness. A similar relationship has also been observed at other bedforms beneath RIS (Schlegel et al., 2022) and merits further investigation.

4.1.2. Moat composition

The seismic reflection profiles in this study do not cross the moat, thus properties in the moat can only be inferred from radar reflectivity. Radar reflectivity indicates at least parts of the moat in the Upstream grid (Fig. 8d) consist of stiff sediment, whereas the moat in the Downstream grid (Fig. 8c) appears to consist of a mosaic of soft and stiff sediment. The existence of stiffer sediment in the moat compared to the bedform is consistent with observations based on radar data (Schlegel et al., 2022) as well as from passive seismic data (Kufner et al., 2021) elsewhere on RIS. Using passive seismic data, areas of enhanced microseismicity e.g., due to stick-slip motion in areas of stiff sediment, can be located. Beneath RIS, microseismic events are located in the troughs between bedforms, while no events are found on the crest of bedforms (Kufner et al., 2021), confirming the existence of stiff sediment in the moat and soft sediment at the bedform crest. Truncated bedforms located upstream of the moat are comprised of soft sediment (Fig. 8b).

4.2. Bedform and moat formation

4.2.1. Bedform formation

We find no evidence for initiation of the SSR formation by ice flow against a topographic seed point. Evidence presented in Smith et al. (2007) show that the neighboring bedform is formed by the deposition of sediment. Similar to the SSR, other bedforms beneath the RIS, including the neighboring bedform, contain a harder upstream end and soft sediment downstream. However, seismic data that would allow us to exclude a competent outcrop or boulder at the upstream end is only available for the SSR. Nevertheless, without further evidence our preferred formation mechanism for the SSR is by the deposition of sediment (Boulton, 1987), which is in accordance with features elsewhere on RIS.

The lack of a topographic seed point indicates either the existence of variations in bed stiffness or instabilities at the ice-bed interface (e.g., Hindmarsh, 1998; Menzies and Shilts, 2002; Fowler, 2010b). We have no evidence that contradicts either of these mechanisms. However, in a similar way to the palaeo record (Piotrowski et al., 2004), bed properties beneath RIS have previously been described as a mosaic of soft and stiff patches (Schlegel et al., 2022). Combining these observations with the variation of bed properties along the crest of the SSR, our preferred interpretation of bedform initiation is inhomogeneities in the subglacial material (Boulton, 1987).

4.2.2. Moat formation

Even though moats can be found without an associated obstacle (Graham and Hogan, 2016), at RIS the location of the moat appears to be associated with the upstream end of the SSR. The moat is an erosional feature, which is underlined by the truncation of bedforms upstream of the moat. In general, the formation of moats is attributed to water flow (Graham and Hogan, 2016; Larter et al., 2019) or enhanced coupling of ice and sediment (Holschuh et al., 2020; Alley et al., 2021). Limited amounts of free water beneath RIS were previously inferred, although not associated with the moat (Murray et al., 2008; Schlegel et al., 2022). Furthermore, under present conditions, we expect significant amounts of water (possibly causing erosion) to be routed into the deeper parts of the bed (Smith et al., 2007) outside of the study area (which is located on a broad central high, see King et al. (2016)). Ice flow against obstacles may cause enhanced melt by pressure melting (Dreimanis, 1993; Lowe and Anderson, 2002). However, we cannot be certain that the moat formed by the action of water under past basal conditions or by enhanced pressure melting, and we have no record of surface flow speed or ice surface elevation changes in recent years (Rignot et al., 2019) that could be linked to large-scale water movement (Wingham et al., 2006). Furthermore, modelling work by Alley et al. (2021) suggests water would route away from the obstacle, resulting in the enhanced coupling of the sediment and ice, causing erosion. However, their modelling suggests scaling of the high-pressure perturbation with obstacle size and a wide continuous moat around the stoss end of the bedform. This geometry of the upstream end of the moat from numerical modelling contradicts to our observations, which includes a bridge and widening of the moat downstream. We have no evidence that the bridge is not a feature that was deposited after the formation of the moat, however, we would expect a high-pressure perturbation that has initially caused the erosion of the moat to be persistent in time and thus inhibiting the deposition of material in the moat.

The sediment in the moat has been interpreted as being stiff, whereas the sediment in the surrounding area, specifically upstream of the moat is soft (in the range of deforming sediment). We therefore expect that the area surrounding the upstream end was composed of soft sediment, which has then been eroded and exposed the stiff material. We have no evidence that this sediment was stiff initially, or if processes during moat formation caused the consolidation of sediment.

Our observations do not validate any of the current theoretical models of moat formation. Since the moat scales with the height of the SSR, and the volume of both is comparable, we favor a formation mechanism where the pressure of the ice flowing against the rigid upstream end causes the erosion. This process is in agreement with the modelling results of Alley et al. (2021). However, the contradictions in the moat shape between the model and our observations suggest that the model must be adapted to the conditions of the RIS (obstacle consisting of a lodged sediment rather than a bedrock outcrop) to fully capture the formation process under the RIS.

4.2.3. Links between deposition of bedforms and erosion of moats

The combination of radar and seismic data allows us to exclude a boulder or outcrop acting as a seed point for bedform and moat initiation. These observations are contrary to recent observations beneath Thwaites Glacier (Muto et al., 2019; Clyne et al., 2020; Alley et al., 2021) as well as the palaeo record (Patterson and Hooke, 1995; Stokes and Clark, 2001) and highlight the diverse mechanisms of moat and bedform initiations. For the SSR beneath RIS we favor the following interpretation. Variations in the subglacial sediment stiffness lead to the deposition of sediment on the initially flat bed (Boulton, 1987). These topographic undulations could then act as seed point for bedform extension by sediment deformation and the erosion of a moat around the seed point. The location and shape of the moat as well as the truncation of bedforms upstream of the moat (red dashed lines in Fig. 3a) imply that erosion of the moat occurred after the formation of at least the upstream end of the SSR, as well as the truncated bedforms. The variation in sediment stiffness along the crest of the SSR, as well as other bedforms beneath RIS (Schlegel et al., 2022) might be attributed to different sediment origins or consolidation of the undulations prior to the deposition of soft sediment in the lee of the undulations. The softening of the sediment along the crest of bedforms occurs at the same distance, regardless of the width of the bedform. Our observations do not allow an interpretation of the processes causing the erosion around the upstream end, but the comparable volume of the SSR and moat at the upstream end (Fig. 5b) implies a feedback of the obstacle size on the depth of the erosion (Schoof and Clarke, 2008). Erosion of soft sediment from the sides expose underlying stiffer material, while the eroded soft sediment is possibly deposited in the lee of the bedform. However, additional sediment supply would be needed to form the SSR along the entire length, as the moat volume is an order of magnitude less than the SSR at the downstream end (Fig. 5a). Even though we cannot determine why the sediment at the upstream end is stiffer than at the downstream end, these observations confirm that sediment can develop sufficient rigidity to withstand erosion and act as a seed point for moat erosion and bedform extension.

4.3. Improved imaging with a 3D processing strategy

The comparison of the Main grid and the Upstream grid confirms that 2D migrated data (that are relatively coarse spaced at 500 m), are sufficient to image the topography in areas where features are aligned in the flow direction. However, data from RIS highlight that when encountering 3D structure, such as the stoss end of a bedform, or small features such as the moat in the Downstream grid, densely spaced profiles and 3D migration are required to remove ambiguity in the data and resolve features that are otherwise not visible. This level of detail is essential to validate models of subglacial bed formation and improve our understanding of active subglacial processes. Similarly, improved basal imaging beneath modern ice streams is essential to validate data from the palaeo record. Interpretation of the palaeo record can be limited by confidence in the timing of feature formation, and for example, whether features form during glaciation or result from subsequent processes, such as weathering.

The denser sampling and 3D migration of the data allowed imaging of steeper topography, such as that shown in Fig. 6. At the stoss end of the SSR, only the 3D migrated radar data allowed imaging of the steep parts, whilst 2D data (seismic and radar) lack clear reflections from the stoss face (Fig. 7d). The absence of a clear reflection in the 2D data can be ascribed to some or all of: (1) weak impedance and permittivity/conductivity contrast between the ice and the sediment at the stoss end of the SSR; (2) limits in the acquisition geometry (insufficient seismic spread length or across-track sampling); or (3) inadequate processing. Due to the existence of a continuous reflection from the stoss side (Fig. 3g), with a dip of 20—45° in the 3D radar data, we expect the coarser acquisition and thus 2D processing to have had a major impact on data quality. The lack of a clear reflection in the 2D data, together with the level of detail revealed from 3D radar data, underlines the importance of 3D surveys and 3D processing to image complex subglacial geometries.

Only the 3D migrated Upstream grid resolves the moat with a bridge, whereas the Main grid implies a depression upstream of the stoss end of the SSR. We assume no temporal change in the topography between the acquisition of the Main grid data in 2016/17 and the Upstream grid in 2017/18, because of the significant amount of sediment that would be required to be moved. Additionally, all lines of the Main grid have been acquired in 2008/09 using the same radar system. An unpublished comparison of these data show no temporal change in bed topography over 9 years. Thus, we attribute the lack of a bridge, and the additional upstream depression observed when comparing Main and Upstream grids, to insufficient sampling of the subsurface and processing limited to a 2D space.

The acquisition and processing of densely spaced lines have allowed us to image the SSR and the moat surrounding it in a level of detail that was unattainable in previous studies of this region. When evaluating theoretical models of bedform and moat formation, high-resolution imaging is essential to establish a true representation of features, such as moat length, continuity of the moat around the upstream end, and the moat-depth to bedform-height relation.

5. Conclusion

Using a regional radar dataset with localized high-resolution 3D radar grids and seismic data we reveal details of a significant subglacial ridge and the surrounding bed, including a moat which is located around the bedform's upstream end. The high-resolution data reveal truncated bedforms, a bridge within the moat, and for the first time resolve the topography and steepness of the bedform and the deep moat surrounding it. Previously, more sparsely sampled data attempted to image the bedform and gave indications of the moat but could not image the moat along its full extend. Only the acquisition of densely spaced radar lines and 3D processing allows imaging of complex basal topography. Detail in the subglacial topography imaged in this study highlight the need for 3D datasets and 3D processing techniques to investigate processes involved in subglacial bedform formation and their chronology. Accurate imaging of complex subglacial geometry and properties can further inform other processes of the subglacial environment.

The lack of a boulder or outcrop at the upstream end of the bedform implies that bedforms beneath Rutford Ice Stream can initiate without pre-existing topography acting as a seed point. The bedform is mostly composed of soft sediment. Lodged sediment at the upstream end represents a stiff obstacle leading to the accumulation of soft sediment in the lee and the erosion of a moat around the upstream end.

Current numerical models of moat erosion cannot reproduce the moat topography, especially the upstream end as well as the length of the moat, observed here. However, using truncated bedforms and the shape of the moat we can reconstruct the chronology of bedform formation, which highlights that the bedform and moat developed at different times with material possibly being reworked from one feature into the other.

Insights into bedform composition and high-resolution topography of the bedforms presented, in combination with basal conditions beneath the Rutford Ice Stream and the observation of an active extension of a bedform in previous studies (Smith et al., 2007; Schlegel et al., 2022), provides valuable insights which will further constrain the processes involved in bedform formation.

CRediT authorship contribution statement

Rebecca Schlegel: Conceptualization, Formal analysis, Methodology, Software, Visualization, Writing – original draft, Writing – review & editing. **Alex M. Brisbourne:** Conceptualization, Formal analysis, Methodology, Software, Supervision, Writing – original draft, Writing – review & editing. **Andrew M. Smith:** Conceptualization, Funding acquisition, Investigation, Methodology, Project administration, Supervision, Writing – review & editing. **Adam D. Booth:** Methodology, Software, Supervision, Writing – review & editing. **Tavi Murray:** Funding acquisition, Project administration, Supervision, Writing – review & editing. **Edward C. King:** Supervision, Writing – review & editing. **Roger A. Clark:** Software, Supervision, Writing – review & editing.

Declaration of competing interest

The authors declare that they have no known competing financial interests or personal relationships that could have appeared to influence the work reported in this paper.

Data availability

The data, which supported the findings of this work (3D bed topography and seismic acoustic impedance), are available via the UK Polar Data Center: https://doi.org/10.5285/11e5449d-2de7-40d8-8994-094238808625 (Schlegel et al., 2024).

Acknowledgements

R. Schlegel was funded by a NERC PhD Studentship through Swansea University (NE/G013187/1). This work was funded by NERC AFI award numbers NE/G014159/1, NE/G013187/1 and NE/F015879/1, and NERC National Capability Science: Strategic Research and Innovation Short Projects. This research contributes to the IMPACT operation which has been part-funded by the European Regional Development Fund through the Welsh Government and Swansea University. Geophysical equipment was provided by NERC's Geophysical Equipment Facility, loan number 887. We thank BAS Operations and N. Gillett for fieldwork support and B. Craven for software support. We also thank R. Alley, R. Larter, K. Hogan, C. Martin and C.D. Hillenbrand for the discussion on this work. University of Leeds acknowledges support of this work by Landmark Software and Services, a Landmark Company and use of SeisSpace/ProMAX via the Landmark University Grant Program, Agreements 2004-COM-024982, 2008-CON-010888 and subsequent renewals. The British Antarctic Survey acknowledges support of this work by Landmark Software and Services, a Landmark Company. We thank the reviewers Sarah Greenwood and Nicholas Holschuh and the Editor Achim Beylich for their excellent feedback, which greatly improved this publication.

References

Alley, R.B., Holschuh, N., MacAyeal, D.R., Parizek, B.R., Zoet, L., Riverman, K., Muto, A., Christianson, K., Clyne, E., Anandakrishnan, S., Stevens, N., Ghost Collaboration, 2021. Bedforms of Thwaites Glacier, West Antarctica: character and Origin. J. Geophys. Res. Earth 126 (12). https://doi.org/10.1029/2021JF006339.

Ashmore, D.W., Bingham, R.G., 2014. Antarctic subglacial hydrology: current knowledge and future challenges. Antarct. Sci. 26 (6), 758–773. https://doi.org/10.1017/S0954102014000546.

Atre, S.R., Bentley, C.R., 1993. Laterally varying basal conditions beneath ice streams B and C, West Antarctica. J. Glaciol. 39 (133), 507–514. https://doi.org/10.1017/S0022143000016403.

Bamber, J.L., Vaughan, D.G., Joughin, I., 2000. Widespread complex Flow in the Interior of the Antarctic Ice Sheet. Science 287 (5456), 1248–1250. https://doi.org/10.1126/science.287.5456.1248.

Barchyn, T.E., Dowling, T.P.F., Stokes, C.R., Hugenholtz, C.H., 2016. Subglacial bed form morphology controlled by ice speed and sediment thickness. Geophys. Res. Lett. 43 (14), 7572–7580. https://doi.org/10.1002/2016GL069558.

Benn, D., Evans, J., 2011. Glaciers and Glaciation. In: Boreas, 2nd edition. Routledge. https://doi.org/10.4324/9780203785010.

Bingham, R.G., Vaughan, D.G., King, E.C., Davies, D., Cornford, S.L., Smith, A.M., Arthern, R.J., Brisbourne, A.M., De Rydt, J., Graham, A.G.C., Spagnolo, M., Marsh, O.J., Shean, D.E., 2017. Diverse landscapes beneath Pine Island Glacier influence ice flow. Nat. Commun. 8 (1), 1618. https://doi.org/10.1038/s41467-017-01597-y.

Booth, A.D., Clark, R.A., Kulessa, B., Murray, T., Carter, J., Doyle, S., Hubbard, A., 2012. Thin-layer effects in glaciological seismic amplitude-versus-angle (AVA) analysis: implications for characterising a subglacial till unit, Russell Glacier, West Greenland. Cryosphere 6 (4), 909–922. https://doi.org/10.5194/tc-6-909-2012.

Boulton, G.S., 1976. The origin of glacially fluted surfaces - observations and theory. J. Glaciol. 17 (76), 287–309. https://doi.org/10.3189/S0022143000013605.

Boulton, G.S., 1987. A theory of drumlin formation by subglacial sediment deformation. In: Drumlin Symposium. Manchester, 1985, pp. 25–80.

Boyce, J.I., Eyles, N., 1991. Drumlins carved by deforming till streams below the Laurentide ice sheet. Geology 19 (8), 787. https://doi.org/10.1130/0091-7613(1991)019<0787:DCBDTS>2.3.CO;2.

Brisbourne, A.M., Smith, A.M., Vaughan, D.G., King, E.C., Davies, D., Bingham, R.G., Smith, E.C., Nias, I.J., Rosier, S.H.R., 2017. Bed conditions of Pine Island Glacier, West Antarctica. J. Geophys. Res. Earth Surf. 122 (1), 419–433. https://doi.org/10.1002/2016JF004033.

Bryce, J., 1833. On the evidences of diluvial action in the north of Ireland. J. Geol. Soc. Dubl. 1, 34–44.

Catania, G.A., Conway, H.B., Gades, A.M., Raymond, C.F., Engelhardt, H., 2003. Bed reflectivity beneath inactive ice streams in West Antarctica. Ann. Glaciol. 36, 287–291. https://doi.org/10.3189/172756403781816310.

Chapwanya, M., Clark, C.D., Fowler, A.C., 2011. Numerical computations of a theoretical model of ribbed moraine formation. Earth Surf. Process. Landf. 36 (8), 1105–1112. https://doi.org/10.1002/esp.2138.

Christoffersen, P., Tulaczyk, S., Behar, A., 2010. Basal ice sequences in Antarctic ice stream: Exposure of past hydrologic conditions and a principal mode of sediment transfer. J. Geophys. Res. 115 (F3), F03034 https://doi.org/10.1029/2009JF001430.

Church, G.J., Bauder, A., Grab, M., Hellmann, S., Maurer, H., 2018. High-resolution helicopter-borne ground penetrating radar survey to determine glacier base topography and the outlook of a proglacial lake. In: 2018 17th International Conference on Ground Penetrating Radar (GPR), pp. 1–4. https://doi.org/10.1109/ICGPR.2018.8441598.

Clark, C.D., 1993. Mega-scale glacial lineations and cross-cutting ice-flow landforms. Earth Surf. Process. Landf. 18 (1), 1–29. https://doi.org/10.1002/esp.3290180102.

Clark, C.D., 2011. Emergent drumlins and their clones: from till dilatancy to flow instabilities. J. Glaciol. 56 (200), 1011–1025. https://doi.org/10.3189/002214311796406068.

Clark, C.D., Hughes, A.L.C., Greenwood, S.L., Spagnolo, M., Ng, F.S.L., 2009. Size and shape characteristics of drumlins, derived from a large sample, and associated scaling laws. Quat. Sci. Rev. 28 (7–8), 677–692. https://doi.org/10.1016/j.quascirev.2008.08.035.

Clark, C.D., Ely, J.C., Spagnolo, M., Hahn, U., Hughes, A.L.C., Stokes, C.R., 2018. Spatial organization of drumlins. Earth Surf. Process. Landf. 43 (2), 499–513. https://doi.org/10.1002/esp.4192.

Clarke, G.K.C., 2005. Subglacial Processes. Annu. Rev. Earth Planet. Sci. 33 (1), 247–276. https://doi.org/10.1146/annurev.earth.33.092203.122621.

Clyne, E.R., Anandakrishnan, S., Muto, A., Alley, R.B., Voigt, D.E., 2020. Interpretation of topography and bed properties beneath Thwaites Glacier, West Antarctica using seismic reflection methods. Earth Planet. Sci. Lett. 550, 116543 https://doi.org/10.1016/j.epsl.2020.116543.

Craig, R.F., 2004. Craig's Soil Mechanics. In: Engineering & Technology, 7th edn. CRC Press. https://doi.org/10.4324/9780203494103.

Dardis, G.F., McCabe, A.M., 1987. In: Rose, J., Menzies, J. (Eds.), Subglacial sheetwash and debris flow deposits in late- Pleistocene drumlins, Northern Ireland. Drumlin Symposium, Balkema, Rotterdam, pp. 225–240.

Dreimanis, A., 1993. Water-eroded crescentic scours and furrows associated with subglacial flutes at Breidamerkurjökull, Iceland. Boreas 22 (2), 110–112. https://doi.org/10.1111/j.1502-3885.1993.tb00170.x.

Dyke, A.S., Morris, T.F., 1988. Drumlin fields, dispersal trains, and ice streams in Arctic Canada. Can. Geogr./Geogr. Can. 32 (1), 86–90. https://doi.org/10.1111/j.1541-0064.1988.tb00860.x.

Ely, J.C., Clark, C.D., Spagnolo, M., Stokes, C.R., Greenwood, S.L., Hughes, A.L.C., Dunlop, P., Hess, D., 2016. Do subglacial bedforms comprise a size and shape continuum? Geomorphology 257, 108–119. https://doi.org/10.1016/j.geomorph.2016.01.001.

Evans, I.S., 1996. Abraded rock landforms (whalebacks) developed under ice streams in mountain areas. Ann. Glaciol. 22, 9–16. https://doi.org/10.3189/1996AoG22-1-9-16.

Finlayson, A., Phillips, E., Benediktsson, Í.Ö., Zoet, L.K., Iverson, N.R., Everest, J., 2019. Subglacial drumlins and englacial fractures at the surge-type glacier, Múlajökull, Iceland. Earth Surf. Process. Landf. 44 (1), 367–380. https://doi.org/10.1002/esp.4485.

Fowler, A.C., 2000. An instability mechanism for drumlin formation. Geol. Soc. Lond. Spec. Publ. 176 (1), 307–319.

Fowler, A.C., 2009. Instability modelling of drumlin formation incorporating lee-side cavity growth. Proc. R. Soc. A. https://doi.org/10.1098/rspa.2008.0490.

Fowler, A.C., 2010a. The formation of subglacial streams and mega-scale glacial lineations. Proc. R. Soc. A: Math. Phys. Eng. Sci. 466 (2123), 3181–3201. https://doi.org/10.1098/rspa.2010.0009.

Fowler, A.C., 2010b. The instability theory of drumlin formation applied to Newtonian viscous ice of finite depth. Proc. R. Soc. A: Math. Phys. Eng. Sci. 466 (2121), 2673–2694. https://doi.org/10.1098/rspa.2010.0017.

Fowler, A.C., Chapwanya, M., 2014. An instability theory for the formation of ribbed moraine, drumlins and mega-scale glacial lineations. Proc. R. Soc. A: Math. Phys. Eng. Sci. 470 (2171), 20140185 https://doi.org/10.1098/rspa.2014.0185.

French, W.S., 1974. Two-dimensional and three-dimensional migration of model-experiment reflection profiles. Geophysics 39 (3), 265–277. https://doi.org/10.1190/1.1440426.

Fuller, S., Murray, T., 2002. Sedimentological investigations in the forefield of an Icelandic surge-type glacier: implications for the surge mechanism. Quat. Sci. Rev. 21 (12−13), 1503–1520. https://doi.org/10.1016/S0277-3791(01)00099-3.

Gades, A.M., Raymond, C.F., Conway, H., Jacobel, R.W., 2000. Bed properties of Siple Dome and adjacent ice streams, West Antarctica, inferred from radio-echo sounding measurements. J. Glaciol. 46 (152), 88–94. https://doi.org/10.3189/172756500781833467.

Gawthorpe, R.L., Fabregas, N., Pechlivanidou, S., Ford, M., Collier, R.E.L., Carter, G.D.O., Mcneill, L.C., Shillington, D.J., 2022. Late Quaternary mud-dominated, basin-floor sedimentation of the Gulf of Corinth, Greece: Implications for deep-water depositional processes and controls on syn-rift sedimentation. October 2021, pp. 1–34. https://doi.org/10.1111/bre.12671.

Goldstein, B., 1994. Drumlins of the Puget Lowland, Washington State, USA. Sediment. Geol. 91 (1–4), 299–311. https://doi.org/10.1016/0037-0738(94)90136-8.

Graham, A.G.C., Hogan, K.A., 2016. Crescentic scours on palaeo-ice stream beds. Geol. Soc. Lond. Mem. 46 (1), 221–222. https://doi.org/10.1144/M46.166.

Graham, A.G.C., Larter, R.D., Gohl, K., Hillenbrand, C.D., Smith, J.A., Kuhn, G., 2009. Bedform signature of a West Antarctic palaeo-ice stream reveals a multi-temporal record of flow and substrate control. Quat. Sci. Rev. 28 (25–26), 2774–2793. https://doi.org/10.1016/j.quascirev.2009.07.003.

Grasmueck, M., Weger, R., Horstmeyer, H., 2005. Full-resolution 3D GPR imaging. Geophysics 70 (1), K12–K19. https://doi.org/10.1190/1.1852780.

Gudmundsson, G.H., 2006. Fortnightly variations in the flow velocity of Rutford Ice Stream, West Antarctica. Nature 444 (7122), 1063–1064. https://doi.org/10.1038/nature05430.

Hanvey, P.M., 1989. Stratified flow deposits in a late Pleistocene drumlin in northwest Ireland. Sediment. Geol. 62 (2–4), 211–221.

Hart, J.K., 1995a. Drumlin formation in Southern Anglesey and Arvon, Northwest Wales. J. Quat. Sci. 10 (1), 3–14. https://doi.org/10.1002/jqs.3390100103.

Hart, J.K., 1995b. Subglacial erosion, deposition and deformation associated with deformable beds. Prog. Phys. Geogr. Earth Environ. 19 (2), 173–191. https://doi.org/10.1177/030913339501900202.

Hart, J.K., 1997. The relationship between drumlins and other forms of subglacial glaciotectonic deformation. Quat. Sci. Rev. 16 (1), 93–107. https://doi.org/10.1016/S0277-3791(96)00023-6.

Hart, J.K., 1999. Identifying fast ice flow from landform assemblages in the geological record: a discussion. Ann. Glaciol. 28, 59–66. https://doi.org/10.3189/172756499781821887.

Hättestrand, C., Kleman, J., 1999. Ribbed moraine formation. Quat. Sci. Rev. 18 (1), 43–61. https://doi.org/10.1016/S0277-3791(97)00094-2.

Heroy, D.C., Anderson, J.B., 2005. Ice-sheet extent of the Antarctic Peninsula region during the Last Glacial Maximum (LGM) - Insights from glacial geomorphology. Bull. Geol. Soc. Am. 117 (11−12), 1497–1512. https://doi.org/10.1130/B25694.1.

Hindmarsh, R.C.A., 1998. Drumlinization and drumlin-forming instabilities: Viscous till mechanisms. J. Glaciol. 44 (147), 293–314. https://doi.org/10.1017/S002214300000263X.

Holschuh, N., Christianson, K., Paden, J., Alley, R.B., Anandakrishnan, S., 2020. Linking postglacial landscapes to glacier dynamics using swath radar at Thwaites Glacier, Antarctica. Geology 48 (3), 268–272. https://doi.org/10.1130/G46772.1.

Ives, L.R.W., Iverson, N.R., 2019. Genesis of glacial flutes inferred from observations at Múlajökull, Iceland. Geology 47 (5), 387–390. https://doi.org/10.1130/G45714.1.

Jones, I., 2014. An Introduction to: Velocity Model Building. EAGE Publications bv. https://doi.org/10.3997/9789073834958

Kerr, M., Eyles, N., 2007. Origin of drumlins on the floor of Lake Ontario and in upper New York State. Sediment. Geol. 193 (1–4), 7–20. https://doi.org/10.1016/j.sedgeo.2005.11.025.

King, E.C., 2020. The precision of radar-derived subglacial bed topography: a case study from Pine Island Glacier, Antarctica. Ann. Glaciol. 61 (81), 154–161. https://doi.org/10.1017/aog.2020.33.

King, E.C., Woodward, J., Smith, A.M., 2007. Seismic and radar observations of subglacial bed forms beneath the onset zone of Rutford Ice Stream, Antarctica. J. Glaciol. 53 (183), 665–672. https://doi.org/10.3189/002214307784409216.

King, E.C., Hindmarsh, R.C.A., Stokes, C.R., 2009. Formation of mega-scale glacial lineations observed beneath a West Antarctic ice stream. Nat. Geosci. 2 (8), 585–588. https://doi.org/10.1038/ngeo581.

King, E.C., Pritchard, H.D., Smith, A.M., 2016. Subglacial landforms beneath Rutford Ice Stream, Antarctica: detailed bed topography from ice-penetrating radar. Earth Syst. Sci. Data 8 (1), 151–158. https://doi.org/10.5194/essd-8-151-2016.

Klages, J.P., Salzmann, U., Bickert, T., Hillenbrand, C.-D., Gohl, K., Kuhn, G., Bohaty, S. M., Titschack, J., Müller, J., Frederichs, T., Bauersachs, T., Ehrmann, W., van de Flierdt, T., Pereira, P.S., Larter, R.D., Lohmann, G., Niezgodzki, I., Uenzelmann-Neben, G., Zundel, M., Dziadek, R., 2020. Temperate rainforests near the South Pole during peak cretaceous warmth. Nature 580 (7801), 81–86. https://doi.org/10.1038/s41586-020-2148-5.

Kufner, S.-K., Brisbourne, A.M., Smith, A.M., Hudson, T.S., Murray, T., Schlegel, R., Kendall, J.M., Anandakrishnan, S., Lee, I., 2021. Not all Icequakes are created Equal: Basal Icequakes Suggest Diverse Bed Deformation Mechanisms at Rutford Ice Stream, West Antarctica. J. Geophys. Res. Earth 126, e2020JF006001. https://doi.org/10.1029/2020JF006001.

Larter, R.D., Hogan, K.A., Hillenbrand, C.-D., Smith, J.A., Batchelor, C.L., Cartigny, M., Tate, A.J., Kirkham, J.D., Roseby, Z.A., Kuhn, G., Graham, A.G.C., Dowdeswell, J.A., 2019. Subglacial hydrological control on flow of an Antarctic Peninsula palaeo-ice stream. Cryosphere 13 (6), 1583–1596. https://doi.org/10.5194/tc-13-1583-2019.

Lemke, R.W., 1958. Narrow linear drumlins near Velva, North Dakota. Am. J. Sci. 256 (4), 270–283. https://doi.org/10.2475/ajs.256.4.270.

Lindsey, J.P., 1989. The Fresnel zone and its interpetive significance. Lead. Edge 8 (10), 33–39. https://doi.org/10.1190/1.1439575.

Lowe, A., Anderson, J., 2002. Reconstruction of the West Antarctic ice sheet in Pine Island Bay during the last Glacial Maximum and its subsequent retreat history. Quat. Sci. Rev. 21 (16–17), 1879–1897. https://doi.org/10.1016/S0277-3791(02)00006-9.

Margold, M., Stokes, C.R., Clark, C.D., Kleman, J., 2015. Ice streams in the Laurentide Ice Sheet: a new mapping inventory. J. Maps 11 (3), 380–395. https://doi.org/10.1080/17445647.2014.912036.

Menzies, J., 1979a. A review of the literature on the formation and location of drumlins. Earth Sci. Rev. 14 (4), 315–359. https://doi.org/10.1016/0012-8252(79)90093-X.

Menzies, J., 1979b. The Mechanics of Drumlin Formation with Particular Reference to the Change in Pore-Water Content of the till. J. Glaciol. 22 (87), 373–384. https://doi.org/10.1017/S0022143000014349.

Menzies, J., Brand, U., 2007. The internal sediment architecture of a drumlin, Port Byron, New York State, USA. Quat. Sci. Rev. 26 (3–4), 322–335. https://doi.org/10.1016/j.quascirev.2006.07.003.

Menzies, J., Shilts, B.W., 2002. Subglacial environments. In: Modern and Past Glacial Environments. Elsevier, pp. 183–278. https://doi.org/10.1016/B978-075064226-2/50011-8.

Monk, D.J., 2010. Fresnel-zone binning: Fresnel-zone shape with offset and velocity function. Geophysics 75 (1), T9–T14. https://doi.org/10.1190/1.3294576.

Morlighem, M., Williams, C.N., Rignot, E., An, L., Arndt, J.E., Bamber, J.L., Catania, G., Chauché, N., Dowdeswell, J.A., Dorschel, B., Fenty, I., Hogan, K., Howat, I., Hubbard, A., Jakobsson, M., Jordan, T.M., Kjeldsen, K.K., Millan, R., Mayer, L., Zinglersen, K.B., 2017. BedMachine v3: complete bed topography and ocean bathymetry mapping of Greenland from multibeam echo sounding combined with mass conservation. Geophys. Res. Lett. 44 (21), 11,051–11,061. https://doi.org/10.1002/2017GL074954.

Murray, T., Smith, A.M., King, M.A., Weedon, G.P., 2007. Ice flow modulated by tides at up to annual periods at Rutford Ice Stream, West Antarctica. Geophys. Res. Lett. 34, L18503 https://doi.org/10.1029/2007GL031207.

Murray, T., Corr, H., Forieri, A., Smith, A.M., 2008. Contrasts in hydrology between regions of basal deformation and sliding beneath Rutford Ice Stream, West Antarctica, mapped using radar and seismic data. Geophys. Res. Lett. 35, L12504 https://doi.org/10.1029/2008GL033681.

Muto, A., Anandakrishnan, S., Alley, R.B., Horgan, H.J., Parizek, B.R., Koellner, S., Christianson, K., Holschuh, N., 2019. Relating bed character and subglacial morphology using seismic data from Thwaites Glacier, West Antarctica. Earth Planet. Sci. Lett. 507, 199–206. https://doi.org/10.1016/j.epsl.2018.12.008.

Newman, W.A., Berg, R.C., Rosen, P.S., Glass, H.D., 1990. Pleistocene Stratigraphy of the Boston Harbor Drumlins, Massachusetts. Quat. Res. 34 (2), 148–159. https://doi.org/10.1016/0033-5894(90)90027-I.

Ó Cofaigh, C., Pudsey, C.J., Dowdeswell, J.A., Morris, P., 2002. Evolution of subglacial bedforms along a paleo-ice stream, Antarctic Peninsula continental shelf. Geophys. Res. Lett. 29 (1199), 41-1–41-44. https://doi.org/10.1029/2001GL014488.

Ó Cofaigh, C., Evans, J., Dowdeswell, J.A., Larter, R.D., 2007. Till characteristics, genesis and transport beneath Antarctic paleo-ice streams. J. Geophys. Res. 112 (F3), F03006 https://doi.org/10.1029/2006JF000606.

Ottesen, D., Stokes, C.R., Rise, L., Olsen, L., 2008. Ice-sheet dynamics and ice streaming along the coastal parts of northern Norway. Quat. Sci. Rev. 27 (9–10), 922–940. https://doi.org/10.1016/j.quascirev.2008.01.014.

Patterson, C.J., Hooke, R. LeB, 1995. Physical environment of drumlin formation. J. Glaciol. 41 (137), 30–38. https://doi.org/10.3189/S0022143000017731.

Piotrowski, J.A., Larsen, N.K., Junge, F.W., 2004. Reflections on soft subglacial beds as a mosaic of deforming and stable spots. Quat. Sci. Rev. 23 (9–10), 993–1000. https://doi.org/10.1016/j.quascirev.2004.01.006.

Rattas, M., Piotrowski, J.A., 2003. Influence of bedrock permeability and till grain size on the formation of the saadjärve drumlin field, Estonia, under an East-Baltic

Weichselian ice stream. Boreas 32 (1), 167–177. https://doi.org/10.1080/03009480310001849.

Raukas, A., Tavast, E., 1994. Drumlin location as a response to bedrock topography on the southeastern slope of the Fennoscandian Shield. Sediment. Geol. 91 (1–4), 373–382. https://doi.org/10.1016/0037-0738(94)90141-4.

Rignot, E., Mouginot, J., Scheuchl, B., van den Broeke, M., van Wessem, M.J., Morlighem, M., 2019. Four decades of Antarctic Ice Sheet mass balance from 1979–2017. Proc. Natl. Acad. Sci. 116 (4), 1095–1103. https://doi.org/10.1073/pnas.1812883116.

Riverman, K.L., Anandakrishnan, S., Alley, R.B., Holschuh, N., Dow, C.F., Muto, A., Parizek, B.R., Christianson, K., Peters, L.E., 2019. Wet subglacial bedforms of the NE Greenland Ice Stream shear margins. Ann. Glaciol. 60 (80), 91–99. https://doi.org/10.1017/aog.2019.43.

Robein, E., 2010. Seismic Imaging: A Review of the Techniques, their Principles, Merits and Limitations, 4. EAGE Education Tour Series.

Rose, J., 1987. Drumlins as part of a glacier bedform continuum. In: Menzies, J., Rose, J. (Eds.), Drumlin Symposium. Balkema, Rotterdam, pp. 103–116.

Schlegel, R., Murray, T., Smith, A.M., Brisbourne, A.M., Booth, A.D., King, E.C., Clark, R. A., 2022. Radar Derived Subglacial Properties and Landforms beneath Rutford Ice Stream, West Antarctica. J. Geophys. Res. Earth 127 (1). https://doi.org/10.1029/2021JF006349.

Schlegel, R., Brisbourne, A., Smith, A., Booth, A. (Eds.), 2024. 3D radar topography, radar-derived bed reflectivity and seismic acoustic impedance of Rutford Ice Stream, West Antarctica, December 2005 to January 2017 (Version 1.0) [Data set]. NERC EDS UK Polar Data Centre. https://doi.org/10.5285/11e5449d-2de7-40d8-8994-094238808625.

Schoof, C.G., Clarke, G.K.C., 2008. A model for spiral flows in basal ice and the formation of subglacial flutes based on a Reiner-Rivlin rheology for glacial ice. J. Geophys. Res.: Solid Earth 113 (B5). https://doi.org/10.1029/2007JB004957.

Shaw, J., Faragini, D.M., Kvill, D.R., Rains, R.B., 2000. The Athabasca fluting field, Alberta, Canada: Implications for the formation of large-scale fluting (erosional lineations). Quat. Sci. Rev. 19 (10), 959–980. https://doi.org/10.1016/S0277-3791(99)00027-X.

Shaw, J., Pugin, A., & Young, R. R. (2008). A meltwater origin for Antarctic shelf bedforms with special attention to megalineations. Geomorphology, 102(3–4), 364–375. doi:https://doi.org/10.1016/j.geomorph.2008.04.005.

Smith, A.M., 1997a. Basal conditions on Rutford Ice Stream, West Antarctica, from seismic observations. J. Geophys. Res. 102 (B1), 543–552.

Smith, A.M., 1997b. Variations in basal conditions on Rutford Ice Stream, West Antarctica. J. Glaciol. 43 (144), 245–255.

Smith, A.M., Murray, T., 2009. Bedform topography and basal conditions beneath a fast-flowing West Antarctic ice stream. Quat. Sci. Rev. 28 (7–8), 584–596. https://doi.org/10.1016/j.quascirev.2008.05.010.

Smith, A.M., Murray, T., Nicholls, K.W., Makinson, K., Adalgeirsdóttir, G., Behar, A.E., Vaughan, D.G., 2007. Rapid erosion, drumlin formation, and changing hydrology beneath an Antarctic ice stream. Geology 35 (2), 127–130. https://doi.org/10.1130/G23036A.1.

Smith, A.M., Anker, P.G.D., Nicholls, K.W., Makinson, K., Murray, T., Rios-Costas, S., Brisbourne, A.M., Hodgson, D.A., Schlegel, R., Anandakrishnan, S., 2021. Ice stream subglacial access for ice-sheet history and fast ice flow: the BEAMISH Project on Rutford Ice Stream, West Antarctica and initial results on basal conditions. Ann. Glaciol. 62 (85–86), 203–211. https://doi.org/10.1017/aog.2020.82.

Spagnolo, M., Clark, C.D., Ely, J.C., Stokes, C.R., Anderson, J.B., Andreassen, K., Graham, A.G.C., King, E.C., 2014. Size, shape and spatial arrangement of mega-scale glacial lineations from a large and diverse dataset. Earth Surf. Process. Landf. 39 (11), 1432–1448. https://doi.org/10.1002/esp.3532.

Stokes, C.R., 2018. Geomorphology under ice streams: moving from form to process. Earth Surf. Process. Landf. 43 (1), 85–123. https://doi.org/10.1002/esp.4259.

Stokes, C.R., Clark, C.D., 2001. Palaeo-ice streams. Quat. Sci. Rev. 20, 1437–1457.

Stokes, C.R., Clark, C.D., 2002. Are long subglacial bedforms indicative of fast ice flow? Boreas 31 (3), 239–249. https://doi.org/10.1111/j.1502-3885.2002.tb01070.x.

Stokes, C.R., Clark, C.D., Lian, O.B., Tulaczyk, S., 2007. Ice stream sticky spots: A review of their identification and influence beneath contemporary and palaeo-ice streams. Earth Sci. Rev. 81 (3–4), 217–249. https://doi.org/10.1016/j.earscirev.2007.01.002.

Stokes, C.R., Spagnolo, M., Clark, C.D., 2011. The composition and internal structure of drumlins: Complexity, commonality, and implications for a unifying theory of their formation. Earth Sci. Rev. 107 (3–4), 398–422. https://doi.org/10.1016/j.earscirev.2011.05.001.

Stokes, C.R., Spagnolo, M., Clark, C.D., Cofaigh, Ó., C., Lian, O. B., & Dunstone, R. B., 2013. Formation of mega-scale glacial lineations on the Dubawnt Lake Ice Stream bed: 1. Size, shape and spacing from a large remote sensing dataset. Quat. Sci. Rev. 77, 190–209. https://doi.org/10.1016/j.quascirev.2013.06.003.

Tulaczyk, S.M., Scherer, R.P., Clark, C.D., 2001. A ploughing model for the origin of weak tills beneath ice streams: a qualitative treatment. Quat. Int. 86 (1), 59–70. https://doi.org/10.1016/S1040-6182(01)00050-7.

Vaughan, D.G., Corr, H.F.J., Smith, A.M., Pritchard, H.D., Shepherd, A., 2008. Flow-switching and water piracy between Rutford ice stream and Carlson inlet, West Antarctica. J. Glaciol. 54 (184), 41–48. https://doi.org/10.3189/002214308784409125.

Verdonck, L., Taelman, D., Vermeulen, F., Docter, R., 2015. The Impact of Spatial Sampling and Migration on the Interpretation of complex Archaeological Ground-penetrating Radar Data. Archaeol. Prospect. 22 (2), 91–103. https://doi.org/10.1002/arp.1501.

Wellner, J.S., Lowe, A.L., Shipp, S.S., Anderson, J.B., 2001. Distribution of glacial geomorphic features on the Antarctic continental shelf and correlation with substrate: Implications for ice behavior. J. Glaciol. 47 (158), 397–411. https://doi.org/10.3189/172756501781832043.

Wingham, D.J., Siegert, M.J., Shepherd, A., Muir, A.S., 2006. Rapid discharge connects Antarctic subglacial lakes. Nature 440 (7087), 1033–1036. https://doi.org/10.1038/nature04660.

Wright, H.E., 1973. Tunnel Valleys, Glacial Surges, and Subglacial Hydrology of the Superior Lobe, Minnesota, pp. 251–276. https://doi.org/10.1130/MEM136-p251.

Wysota, W., 1994. Morphology, internal composition and origin of drumlins in the southeastern part of the Chelmno-Dobrzyń Lakeland, North Poland. Sediment. Geol. 91 (1–4), 345–364. https://doi.org/10.1016/0037-0738(94)90139-2.

Yilmaz, Ö., 2001. Seismic Data Analysis. In: Investigations in Geophysics, Vol. 10 (2 volu. Society of Exploration Geophysicists. https://doi.org/10.1190/1.9781560801580.

Zelčs, V., Dreimanis, A., 1997. Morphology, internal structure and genesis of the Burtnieks drumlin field, Northern Vidzeme, Latvia. Sediment. Geol. 111 (1–4), 73–90. https://doi.org/10.1016/S0037-0738(97)00007-9.

Zhao, W., Forte, E., Colucci, R.R., Pipan, M., 2016. High-resolution glacier imaging and characterization by means of GPR attribute analysis. Geophys. J. Int. 206 (2), 1366–1374. https://doi.org/10.1093/gji/ggw208.